ELEMENTA
Science of the Anthropocene

Salganik, E, et al. 2023. Temporal evolution of under-ice meltwater layers and false bottoms and their impact on summer Arctic sea ice mass balance. *Elem Sci Anth*, 11: 1. DOI: https://doi.org/10.1525/elementa.2022.00035

RESEARCH ARTICLE

Temporal evolution of under-ice meltwater layers and false bottoms and their impact on summer Arctic sea ice mass balance

Evgenii Salganik[1,*], Christian Katlein[2], Benjamin A. Lange[3], Ilkka Matero[2,4], Ruibo Lei[5], Allison A. Fong[2], Steven W. Fons[6], Dmitry Divine[3], Marc Oggier[3,7], Giulia Castellani[2], Deborah Bozzato[8], Emelia J. Chamberlain[9], Clara J. M. Hoppe[2], Oliver Müller[10], Jessie Gardner[11], Annette Rinke[2], Patric Simões Pereira[12], Adam Ulfsbo[12], Chris Marsay[13], Melinda A. Webster[14], Sönke Maus[1], Knut V. Høyland[1], and Mats A. Granskog[3]

Low-salinity meltwater from Arctic sea ice and its snow cover accumulates and creates under-ice meltwater layers below sea ice. These meltwater layers can result in the formation of new ice layers, or false bottoms, at the interface of this low-salinity meltwater and colder seawater. As part of the Multidisciplinary drifting Observatory for the Study of the Arctic Climate (MOSAiC), we used a combination of sea ice coring, temperature profiles from thermistor strings and underwater multibeam sonar surveys with a remotely operated vehicle (ROV) to study the areal coverage and temporal evolution of under-ice meltwater layers and false bottoms during the summer melt season from mid-June until late July. ROV surveys indicated that the areal coverage of false bottoms for a part of the MOSAiC Central Observatory (350 by 200 m^2) was 21%. Presence of false bottoms reduced bottom ice melt by 7–8% due to the local decrease in the ocean heat flux, which can be described by a thermodynamic model. Under-ice meltwater layer thickness was larger below first-year ice and thinner below thicker second-year ice. We also found that thick ice and ridge keels confined the areas in which under-ice meltwater accumulated, preventing its mixing with underlying seawater. While a thermodynamic model could reproduce false bottom growth and melt, it could not describe the observed bottom melt rates of the ice above false bottoms. We also show that the evolution of under-ice meltwater-layer salinity below first-year ice is linked to brine flushing from the above sea ice and accumulating in the meltwater layer above the false bottom. The results of this study aid in estimating the contribution of under-ice meltwater layers and false bottoms to the mass balance and salt budget for Arctic summer sea ice.

Keywords: Salinity, Meltwater, Sea ice, False bottom, Ice melt, MOSAiC

Introduction

During Arctic summer, sea ice warms, ablates from both the surface and bottom, and loses salt. Snow and ice melt results in the accumulation of low-salinity meltwater. Most of this meltwater is transferred to the ocean (Eicken et al., 2002), while some of it migrates to surface melt

[1] Norwegian University of Science and Technology, Trondheim, Norway
[2] Alfred-Wegener-Institut Helmholtz-Zentrum für Polar- und Meeresforschung, Bremerhaven, Germany
[3] Norwegian Polar Institute, Fram Centre, Tromsø, Norway
[4] Svalbard Integrated Arctic Earth Observing System Knowledge Centre, Longyearbyen, Svalbard
[5] Key Laboratory for Polar Science of MNR, Polar Research Institute of China, Shanghai, China
[6] Earth System Science Interdisciplinary Center, University of Maryland, College Park, MD, USA
[7] International Arctic Research Center, University of Alaska Fairbanks, Fairbanks, AK, USA
[8] Groningen Institute for Evolutionary Life Sciences, University of Groningen, Groningen, The Netherlands
[9] Scripps Institution of Oceanography, University of California, San Diego, CA, USA
[10] University of Bergen, Bergen, Norway
[11] The Arctic University of Norway, Tromsø, Norway
[12] Department of Marine Sciences, University of Gothenburg, Gothenburg, Sweden
[13] Skidaway Institute of Oceanography, University of Georgia, Savannah, GA, USA
[14] Geophysical Institute, University of Alaska Fairbanks, Fairbanks, AK, USA

* Corresponding author:
Email: salganikea@gmail.com

ponds, the sea ice matrix, and under-ice meltwater layers (Untersteiner, 1968). When surface ponds drain, or meltwater from ice-bottom melt accumulates below ice, the formation of new ice, so called "false bottoms," can be promoted at the interface between the fresher and more saline water. False bottoms form due to a substantial difference in freezing temperatures of water with different salinities. Such ice formation in summer was observed long ago by Nansen (1897). The modeling of false bottom growth has been described by Notz et al. (2003) and Alexandrov and Nizovtseva (2008), where the false bottoms usually form in under-ice melt ponds, protected from mixing by under-ice features like ridges. Tsamados et al. (2015) estimated a reduction in bottom melt rates by false bottoms using the CICE model. Smith (2018) presented a thermodynamic model of false bottoms and under-ice melt ponds accounting for the effects of ice thickness, meltwater salinity, and brine rejection from both ice and false bottoms. In that model, the presence of false bottoms could reduce ice bottom melt by 1–8% by insulating the sea ice from the ocean.

Until recently, the most comprehensive Arctic drift experiment with combined measurements of sea ice, atmosphere, and ocean was conducted by the Surface Heat Budget of the Arctic Ocean (SHEBA, October 1997–1998) expedition in the region of the Beaufort Gyre. SHEBA showed sea ice evolution during growth and decay periods with extensive mass balance and albedo measurements (Perovich et al., 2003). The mean salinity of false bottoms during SHEBA was 0.4 ± 0.4 ($n = 35$), while the average under-ice meltwater layer thickness was 35–47 cm during June–August (Eicken et al., 2002). Eicken (1994) reported salinity of the under-ice meltwater layer of 1.5 and a layer thickness of 0.31 m, with false bottom salinity of 1.0 and mean thickness of 0.2 m during the ARCTIC 91 expedition in the central Arctic. He also observed significant differences in salinity profiles of level ice with (0.4–0.7) and without (3.1) an under-ice meltwater layer, indicating desalination by meltwater flushing. False bottoms were found at 5% of extracted cores during ARCTIC 91, 10% of cores in the Beaufort Sea (Jeffries et al., 1995), 15% during SHEBA (Perovich et al., 2003), and 50% at the drifting station Charlie (Hanson, 1965), thus appearing to be a recurring process of ice formation in summer. During the Multidisciplinary drifting Observatory for the Study of the Arctic Climate (MOSAiC), false bottom areal fraction was estimated to have been 20% using ice drilling (Smith et al., 2022). The drilling was performed along five lines and included 132 holes during July 14–29, 2020. In this study, we used sonar measurements to map the extent of false bottoms and under-ice meltwater layers, which allowed analysis of their temporal evolution and the environmental conditions for false bottom formation, while ice coring and ice mass balance (IMB) buoys allowed investigation of the temporal evolution of their physical parameters.

Salinity and temperature of under-ice meltwater is controlled by both ice melt and desalination (Smith, 2018). The physical properties of sea ice, including thickness, temperature, salinity, and density, also affect its surface albedo (Perovich and Grenfell, 1981), the transfer of solar radiation through the ice (Maykut, 1986), and its mechanical and thermodynamic properties (Timco and Weeks, 2010). Knowing these physical properties is vital for almost any modelling of physical, chemical, or biological processes in the Arctic (Weeks, 2010), especially for the energy balance of sea ice and its interactions with the atmosphere and ocean, and for biogeochemical processes. Sea ice physical properties vary across multiple spatial and temporal scales, and their evolution depends on many other factors, including atmospheric and oceanic conditions, precipitation, ice motion and dynamics, and ice floe geographical position. Only with knowledge of sea ice salinity, temperature and density can we estimate the solid ice fraction of sea ice (Assur, 1960) and connect freeboard measurements to the ice thickness, which can improve ice thickness retrievals from satellite data. Ice salinity plays a significant role in ice mass balance, and salinity variations are responsible for a total ice volume increase of 10% via changes in the specific heat capacity and the energy of melting (Vancoppenolle et al., 2009). Fluxes of salt and meltwater during sea ice melt have a strong impact on salinity stratification of the Arctic Ocean, which can affect thermohaline circulation (Aagaard and Carmack, 1989). Ice physical properties also affect the productivity of ice algae and sea ice biogeochemical processes (Manes and Gradinger, 2009).

The first targeted study of salinity evolution during the melt period was performed by Malmgren (1927) in drift ice during the Maud expedition. Wang et al. (2020) presented variability of physical properties of late summer drifting ice in the Pacific sector of the Arctic Ocean during August 2008–2018, with average salinities of 1.9 for first-year ice (FYI) and 1.3 for multiyear ice. Notz and Worster (2008) described the main desalination processes as gravity drainage and flushing of surface meltwater and melt ponds. During winter, desalination is governed mostly by gravity drainage (Untersteiner, 1968), while flushing becomes important during summer. Ice permeability is a controlling factor for gravity drainage, increasing with temperature as the ice warms (Golden et al., 1998). Furthermore, gravity drainage has been successfully modeled using a 1-D sea ice model and can be triggered both by atmospheric heat and bottom melt from oceanic heat (Griewank and Notz, 2013), while Vancoppenolle et al. (2007) formulated the first parametrization of the ice flushing mechanism.

This paper describes the areal coverage of under-ice meltwater layers, and the evolution of their thickness and salinity during the summer melt period from May to July. It links ice bottom topography to the formation of such meltwater layers and highlights the importance of ridges. The mass balance of the melt is then examined, including the evolution and effects of under-ice meltwater layers as well as false bottoms, by combining data from in situ measurements, ice mass balance (IMB) buoys and remotely operated vehicle (ROV) multibeam sonar. We further show observations of thickness and salinity of false bottoms and compare their observed growth and melt with a thermodynamic model. Finally, we present the evolution of physical properties of undeformed FYI and second-year ice (SYI) at the MOSAiC Central Observatory floe during the melt season,

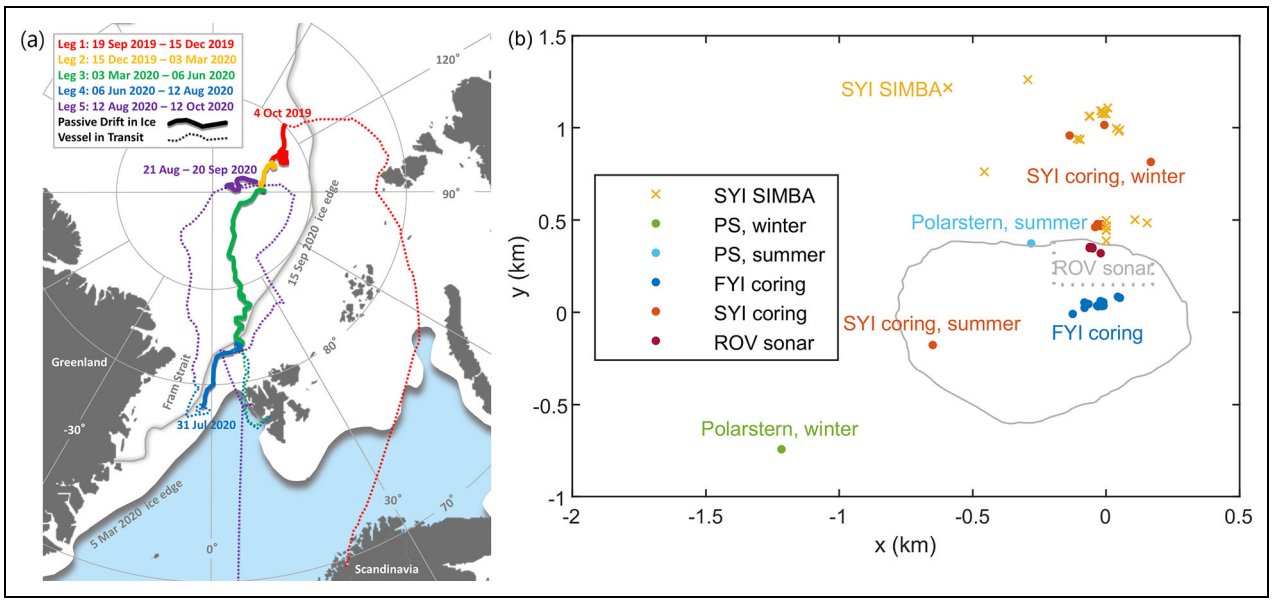

Figure 1. Locations of the Central Observatory and the main observation sites during MOSAiC. (a) Locations of the drifting Central Observatory (solid) and *Polarstern* cruise track (dotted) during MOSAiC, with the sea ice edge at the annual maximum and minimum, from Shupe et al. (2020), and (b) locations of first-year ice (FYI) and second-year ice (SYI) coring sites, the remotely operated vehicle (ROV) sonar scan area, and *Polarstern* relative to the snow ice mass balance array (SIMBA) buoys in the MOSAiC Central Observatory during summer 2020, with the FYI SIMBA buoy at (0,0). The gray line represents Central Observatory floe outlines for July 22, 2020.

showing how they are coupled with physical properties of under-ice meltwater layers.

Materials and methods

Expedition

Nicolaus et al. (2022) presents an overview of snow and ice work during the MOSAiC expedition, which took place in 2019–2020 with the aim to better understand the coupled ice, ocean, and atmosphere system and the sea ice mass and energy budget. The MOSAiC study area consisted of two regions: the Central Observatory, mainly including the area around the ship, and the Distributed Network, which consisted of remote sites in a 40-km radius around the Central Observatory. In brief, in September 2019, the icebreaker *Polarstern* (Knust, 2017) traveled through the northern Laptev Sea and moored itself inside the ice pack on October 4, 2019. Thereafter the Central Observatory was established, including the establishment of coring sites, ROV sites and deployment of IMBs. This observatory drifted for 10 months across the central Arctic, following the Transpolar Drift, until it reached the ice edge in Fram Strait on July 31, 2020 (**Figure 1a**). The sea ice of the Central Observatory around *Polarstern* was formed in a polynya north of the New Siberian Islands in December 2018 (Krumpen et al., 2020). The initial size of the floe was 2.8 km by 3.8 km, with a strongly deformed part in its center, and decreased to 0.9 km^2 in June 2020. The residual ice (which eventually became SYI), that was formed in December 2018 and remained at the start of the drift, had a modal thickness of 0.37 m on September 25, 2019, based on a series of in situ measurements conducted within the Distributed Network. The Central Observatory drifted from the central Arctic Ocean to the marginal ice zone during May–July 2020 (Lei et al., 2022). Rinke et al. (2021) analyzed meteorological conditions during MOSAiC and found that most atmospheric variables and months were typical, except for above-normal temperatures and total column water vapor in May–August.

ROV multibeam sonar

An ROV (M500, Ocean Modules, Sweden) equipped with a number of scientific sensors including multibeam sonar (DT-101, Imagenex, Canada) was used for under-ice surveys, including measuring the ice draft in the vicinity of the FYI coring site (Katlein et al., 2017). Seven scans were performed during the melt season between June 24 and July 28, close to the Central Observatory floe edge, covering an area with undeformed ice and several ice ridges (**Figure 1a**). ROV multibeam sonar scans covered an area of approximately 350 by 200 m^2 in diameter and were processed with a horizontal resolution of 0.5 m. The modal draft of open water areas was used as a reference level with zero draft. Draft of different types of ice, including FYI and SYI with and without false bottoms, was found using ROV scans for chosen representative locations. In this study we use ROV multibeam sonar to classify areas with the presence of false bottoms and to estimate melt rates of FYI and SYI without false bottoms. Areas with the presence of false bottom were identified as ones with ice draft increase during July 1–14, when ice at coring and IMB buoy sites was already melting.

Ice coring

ROV multibeam sonar can give detailed information about bottom ice melt in areas without false bottoms, but is

unable to provide such information where false bottoms are present. To fill this observational gap, we used ice coring, performed in the FYI area with observations of false bottoms. A regular weekly program of measurements, including ice coring, was performed over the duration of the expedition by team ICE (Nicolaus et al., 2022). In this study, we present the results from ice coring of two types of undeformed level ice during the melt period. Ice properties from the MOSAiC coring program before the melt season are described by Angelopoulos et al. (2022). One coring site was established on FYI and a second on SYI that had survived the previous summer and was the oldest ice at the start of the drift. The ice cores were extracted with 9-cm (Mark II) and 7.25-cm (Mark III) internal diameter ice corers (Kovacs Enterprise, US). Cores were obtained within 2 m of each other during a single coring day. The weekly planned coring activities were performed at the respective coring locations within 130 m and 50 m to each other for FYI and SYI, respectively. The SYI coring site had to be re-located by a distance of about 1.0 km in June 2020 (**Figure 1b**) to a location with similar ice to the first SYI site.

During each coring event, ice temperature was measured in situ from a separate temperature core, using Testo 720 thermometers in drill holes with a length of half-core-diameter at 5-cm vertical resolution. Ice bulk salinity was measured from melted sections of a designated salinity core using a YSI 30 conductivity meter with 5-cm vertical resolution (the conductivity is converted to salinity and reported on the Practical Salinity Scale 1978, PSS-78, which is dimensionless). Ice density was measured using the hydrostatic weighing method (Pustogvar and Kulyakhtin, 2016) from density cores in the freezer laboratory onboard *Polarstern*. Relative volumes of brine and gas were estimated from ice salinity, temperature and density using Cox and Weeks (1983) for cold ice and Leppäranta and Manninen (1988) for ice warmer than −2°C. The ice thickness and draft were measured manually for 20–30 ice cores during each coring session for each type of ice; in this study we present average values (± standard deviation) for each coring site. The meteoric water content for FYI, under-ice meltwater layer, melt ponds and false bottoms was estimated using measurements of salinity and stable oxygen isotopic composition from Smith et al. (2022).

According to von Albedyll et al. (2021), airborne electromagnetic (EM) measurements for the period between June 21 and July 1 in the Distributed Network give the combined snow and ice thickness with a mean of 2.5 m and mode of 2.1 m. Visual inspection of the satellite imagery of the Central Observatory (Webster et al., 2022) indicate that FYI occupied around 30% of the Central Observatory on June 30, 2020, while 70% was covered by SYI. The maximum weekly average thickness of undeformed FYI and SYI at coring sites was 1.62 m and 2.33 m, respectively, which gives a mean thickness of undeformed ice of 2.1 m. These findings suggests that the chosen coring sites were representative for the MOSAiC Distributed Network, as the mean thickness of undeformed FYI and SYI is similar to the modal thickness from the EM measurements.

During melt season, sea ice produces meltwater from surface and bottom melt and transfers brine downwards. Ice coring provides complete data for calculating the one-dimensional salt and meltwater balance. The under-ice meltwater sources are snow melt Δh_s and ice melt Δh_i. The salt originates from melting sea ice with a salinity S_i and ice salinity change ΔS_i due to brine drainage or flushing, which we assume only during the presence of a false bottom. Without the presence of false bottom, heavier brine is transferred from sea ice directly to the ocean due to its higher density (Peterson, 2018). We estimated the meltwater layer bulk salinity S_{mw} as:

$$S_{mw} = \frac{\rho_{si}(S_i \Delta h_i + \Delta S_i h_i)}{\rho_{si} \Delta h_i + \rho_s \Delta h_s}, \quad (1)$$

where ρ_{si} is the sea ice density, and ρ_s is the snow density (330 kg m^{-3}).

Here we do not consider brine rejection from the false bottom, which will partly accumulate in the under-ice meltwater layer, nor do we consider possible lateral transport of meltwater from other ice types. To validate this estimate of meltwater layer salinity, we used the brine salinity of the bottom 5 cm of ice cores, which we extracted using a centrifuge shortly after the coring.

The amount of grown or melted ice h_i depends on the sum of the conductive heat flux q_c and the ocean heat flux q_w, and can be expressed as

$$-\rho_{si} L_{si} \partial \eta_i / \partial t = q_c + q_w, \quad (2)$$

whereL_{si} is the effective latent heat of sea ice, and t is the time.

The conductive heat flux q_c depends on the ice or snow top and bottom temperatures T_{top} andT_{bot}, and its thickness $h_{i,s}$ according to Fourier's law:

$$q_c = -k_{si,s} \partial T / \partial Z \cong \kappa_{si,s} (T_{top} - T_{bot}) / h_{i,s}, \quad (3)$$

where $k_{si,s}$ is the sea ice or snow thermal conductivity, and $\partial T / \partial Z$ is the vertical temperature gradient.

Interface temperatures of false bottoms were measured by FYI snow ice mass balance array (SIMBA) buoys. Ice coring provides values of false bottom thickness, which we used to validate the thermodynamic model by Alexandrov and Nizovtseva (2008). This model requires measurements of seawater temperature, salinity and friction velocity. Ice-ocean friction velocity was estimated based on the 6-hour average ice drift velocity measurements from *Polarstern* using ice-ocean drag coefficient C_d, while seawater physical parameters were measured by the *Polarstern* thermosalinograph at a depth of 11 m. The estimated values of ice-ocean friction velocity and drag coefficient were compared with in situ measurements from vertical microstructure profiler by Fer et al. (2022). For false bottom modelling, the physical parameters of sea ice were taken from Alexandrov and Nizovtseva (2008).

Ice mass balance buoys

In order to study the temporal evolution of thickness and temperature of the under-ice meltwater layer, we used non-destructive temperature measurements from ice mass

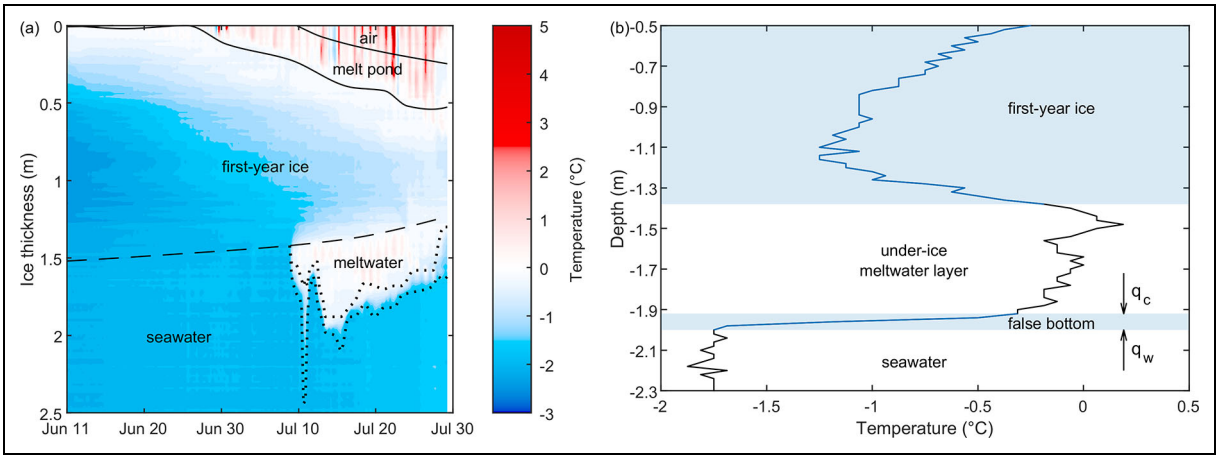

Figure 2. Temperature evolution and vertical temperature profile from FYI SIMBA. (a) Interfaces were found using both heating and in situ temperatures from first-year ice (FYI) sea ice mass balance array (SIMBA) buoys. The layer between meltwater and seawater shown by dotted lines represents the estimate of false bottom, identified by a substantial vertical temperature gradient. Black dashed line is for the bottom of the sea ice. A zero-reference level was set at the snow-ice interface. (b) A typical temperature profile in the presence of a false bottom measured by FYI SIMBA on July 13, 2020.

balance buoys. At both common coring sites of the MOSAiC Central Observatory, one ice-mass balance buoy (SIMBA, SAMS Enterprise Ltd, UK) was deployed on October 29, 2019. The distance between coring sites and SIMBA locations was less than 150 m (**Figure 1b**). SIMBAs have a chain of 5 m, with sensor spacing of 2 cm, and provide temperature readings every 6 hours with accuracy of 0.1°C. Daily heating cycles of internal heating of 30 s and 120 s allow to identify the location of snow-ice and ice-water interfaces with high precision (Jackson et al., 2013). Lei et al. (2022) presented an overview of SIMBA buoys deployed over the MOSAiC Distributed Network. We identified the under-ice meltwater as a layer with temperature higher than that of the underlaying seawater. We separated this meltwater layer into two parts: a near-isothermal upper one and a lower one with a strong vertical temperature gradient, corresponding to estimated false bottom location (**Figure 2**). At coring sites, the under-ice meltwater layer thickness was estimated as the observed distance between the ice draft and the draft of the false bottom.

We investigated properties of sea ice with and without surface melt ponds. Coring was always performed at unponded areas (not allowing vertical meltwater transfer), while FYI and SYI SIMBAs were located in surface melt ponds. The estimated maximum melt pond depth at the SIMBA sites was 30 cm for FYI and 33 cm for SYI, before SIMBAs stopped responding in early August. The average melt pond depths at transects measured using Magnaprobe in late July were 22 cm for FYI and 29 cm for SYI (Webster et al., 2022).

The advantage of SIMBA data is that they allow for the delineation of surface and bottom melt, though the freeboard is unknown (**Figure 2a**). We estimated the freeboard for SIMBA measurements from the snow and ice thickness estimates from SIMBAs, as well as snow and ice density. For these estimates, we assumed snow density as 330 kg m^{-3}, while sea ice density was estimated from in situ measurements of ice salinity, temperature, and density measurements in laboratory conditions. Ice core properties are influenced by spatial variability, but the large number of cores (20–30) allowed us to limit this effect for FYI. Thickness values from discrete SYI cores had much higher variability. To estimate the water level for SIMBAs, we assumed equal bottom melt for the coring site and the corresponding SIMBA. This approach gives the difference between surface melt for ponded (SIMBA) and not ponded (coring) areas, which is equivalent to the water level change of undrained melt ponds at the SIMBA sites.

Results

Defining the melt season

To define a duration of the melt season, estimating the timing of the main events related to the melt processes is important. In the following are the main thermal events at FYI and SYI coring sites based either on observations at the coring sites, SIMBAs or *Polarstern* air and water temperature records (see also **Figure 3**):

Day 1: May 10, 2020—snow melt onset and air warming event up to −1°C
Day 16: May 25, 2020—air temperature reaches 0°C, first FYI surface melt ponds and FYI bottom melt (SIMBA)
Day 28: June 6, 2020—first SYI bottom melt (SIMBA)
Day 32: June 10, 2020—FYI melt ponds refreeze (SIMBA); seawater temperature increases
Day 38: June 16, 2020—first under-ice meltwater layers observed at SYI SIMBA site
Day 44: June 22, 2020—first melt ponds observed at SYI SIMBA site
Day 49: June 27, 2020—previously refrozen melt ponds at FYI SIMBA site melt again

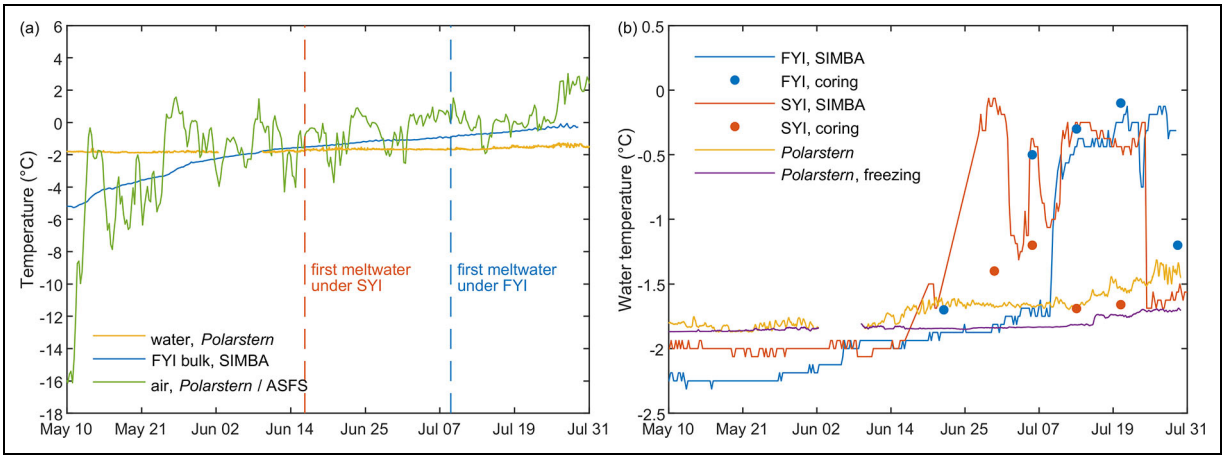

Figure 3. Evolution of air, ice, and water temperatures. (a) The 6-hour mean air temperature from *Polarstern*, first-year ice (FYI) bulk temperature from sea ice mass balance array (SIMBA) over the whole ice column, in situ water temperature from the *Polarstern* thermosalinograph at 11-m depth, and (b) ice bottom temperature from SIMBA and coring sites, in situ water temperature and freezing temperature estimated from salinity measurements from the *Polarstern* thermosalinograph at 11-m depth. While *Polarstern* left the MOSAiC floe from mid-May to mid-June 2020, air temperature measurements were provided by an Atmospheric Surface Flux Station (ASFS).

Day 61: July 9, 2020—first under-ice meltwater layer and rapid surface melt of FYI (SIMBA)

On March 5, the lowest FYI (−12.0°C) and SYI (−11.2°C) bulk temperatures were measured by SIMBAs, after which both air and ice temperatures started to increase. In the middle of May, the air temperatures reached the freezing point of seawater, which also corresponded with the end of ice growth. Two weeks later at the end of May, there was an indication of the first melt pond formation and first bottom melt. By June 10, melt ponds at the FYI SIMBA site refroze, while FYI melt ponds at the Central Observatory were already frozen and snow-covered since June 5–6 based on satellite imagery (Webster et al., 2022). The seawater temperature, measured at *Polarstern* by thermosalinograph at 11-m depth, started to deviate more strongly from the freezing point from June 10 onwards. Substantial FYI bottom melt was observed by both coring and the SIMBA from June 22 onwards. In mid-July there was a significant increase in ice melt rate as the Central Observatory approached the ice edge in Fram Strait (Shupe et al., 2022). In this paper we focus on the development of under-ice meltwater layers formed in mid-June at the SYI SIMBA site and in mid-July at the FYI coring and SIMBA sites.

Under-ice meltwater layers

Areal coverage

We used seven ROV scans of ice bottom topography performed between June 24 and July 28 covering 0.07 km^2 area of the Central Observatory to evaluate the areal coverage of false bottoms and under-ice meltwater layers. We identified FYI areas with false bottoms (shown as blue-shaded areas in **Figure 4a**) as those with ice draft increase during the period July 1–14. The draft in the highlighted false bottom area was at first increasing and then decreasing, also becoming more spatially homogeneous. **Figure 4b** illustrates the temporal evolution of ice draft along a selected cross-section, with ice draft increase between June 28 and July 7 where false bottoms were identified. During July 1–14, the largest highlighted area with false bottoms experienced average draft increase by 0.33 ± 0.10 m, while the draft of FYI without false bottoms decreased by 0.31 ± 0.06 m. FYI at the coring site also experienced a decrease in draft by 0.27 ± 0.08 m (n = 22) between June 22 and July 13. The areal fraction of false bottoms within the part of Central Observatory scanned by ROV was 21% on July 14 (350 by 200 m^2), which is in agreement with 20% estimation by ice drilling from Smith et al. (2022).

Our analysis suggests that the accumulation of under-ice meltwater occurs in the areas with thinner ice, surrounded by ridges. FYI without false bottoms was not surrounded by ice ridges unlike the false bottom area. The chosen location with ice draft below 1.7 m had over half of its area covered with false bottoms (**Figure 4a**).

Temporal evolution of under-ice meltwater layers

ROV sonar measurements allowed us to estimate areas with false bottoms on July 14, but not the thickness of the under-ice meltwater layer, because the FYI above it also melts and moves the upper boundary of under-ice meltwater layer upwards. For the largest under-ice meltwater accumulation area bounded by the −1.7 m draft isoline (**Figure 4a**), the average under-ice meltwater layer thickness was estimated to be at least 0.33 m, as the melt of FYI above it is not known. This estimate is based on the difference between ice draft before false bottom formation on July 1 and the maximum draft of false bottoms on July 14. After July 14, the meltwater presumably reached the bottom of under-ice pools, protected by ice ridges, surrounding the FYI area. Following that event, the false bottoms started to migrate upwards, and rates of this migration were similar to the melt rates of FYI without

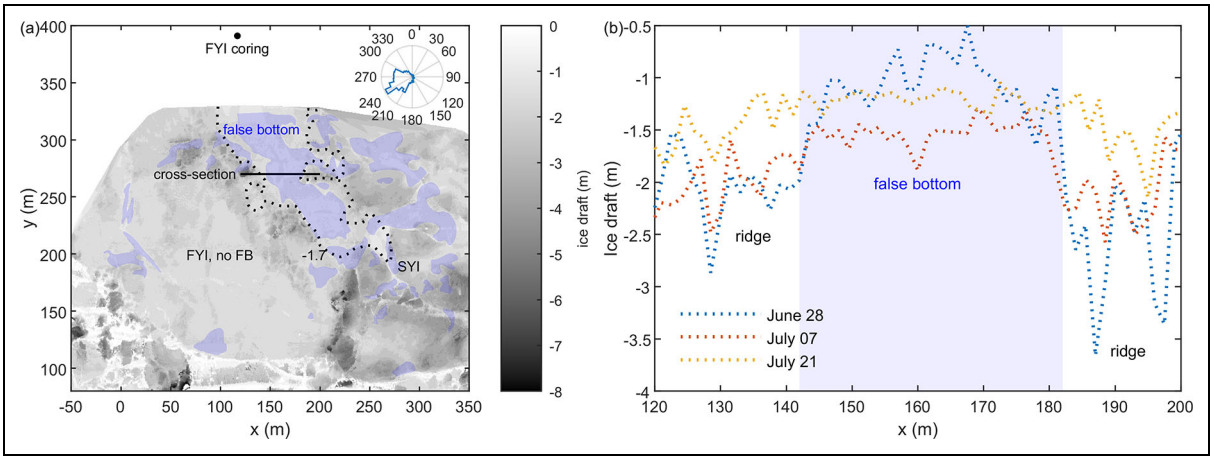

Figure 4. Ice bottom topography and ice draft for the chosen cross-section. (a) Ice bottom topography on July 1, 2020, measured by remotely operated vehicle sonar, showing estimated locations of false bottoms (FB, blue-shaded areas), −1.7 m draft isoline around the largest false bottom area (dotted line), location of first-year ice (FYI) and second-year ice (SYI) without false bottoms, and the FYI coring site, and (b) ice draft for the cross-section at y = 270 m in (a) on various dates. The polar histogram in (a) shows frequency of ice drift direction in relation to the displayed ice floe orientation, with prevailing drift in southwest direction (250°; Schmithüsen, 2021).

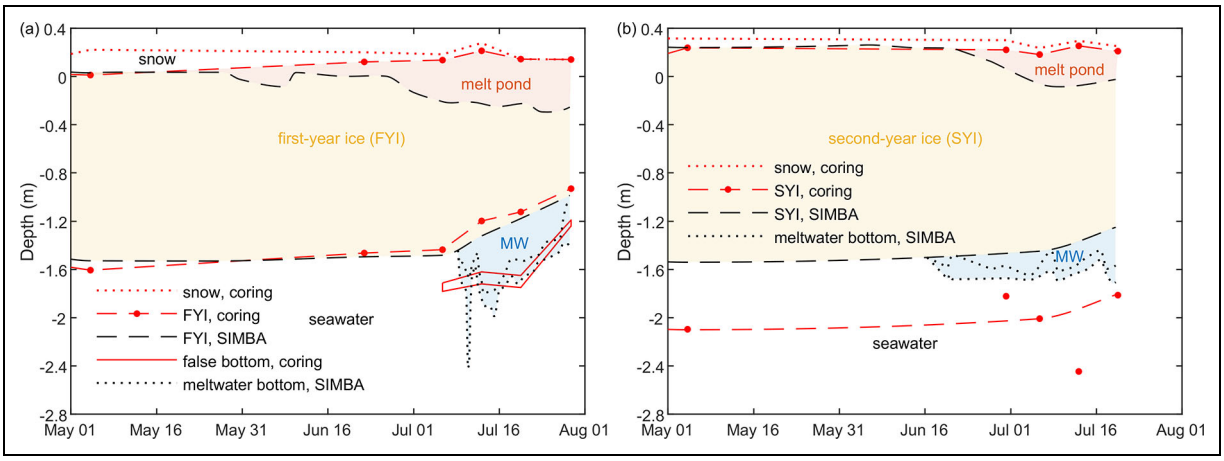

Figure 5. Depth evolution of snow, sea ice, meltwater, and false bottoms during melt season. Depth of snow, sea ice, meltwater (MW), and false bottom interfaces from coring and from sea ice mass balance arrays (SIMBAs) for (a) first-year ice (FYI) and (b) second-year ice (SYI). The depth for SIMBAs was estimated with an assumption of equal bottom melt for coring and for SIMBAs sites. The layer between meltwater and seawater shown by dotted lines represents the estimate of false bottom location, identified by a significant vertical temperature gradient as in **Figure 2b**.

false bottoms. A more precise estimate of temporal evolution of under-ice meltwater layers was made by using the temperature measurements from SIMBAs and ice draft measurements from ice coring (**Figure 5**). We observed the presence of an under-ice meltwater layer at the FYI coring site, and at both FYI and SYI SIMBAs. At the FYI coring site, the meltwater was observed three days earlier than at the FYI SIMBA. Despite the 130-m distance between the two sites and the different surface topography (the SIMBA site was ponded, and the FYI coring site was unponded), their estimates of meltwater thickness were similar (**Figure 5a**).

The thickness of the FYI under-ice meltwater layer at the FYI coring site was in the range of 26–54 cm with the average thickness of 45 ± 15 cm (n = 4), while the average thickness of that layer at the FYI SIMBA was 47 ± 14 cm (n = 81; **Figure 5a**). By combining ROV measurements of false bottom draft and FYI draft for July 1–14 with coring measurements of false bottom thickness, we can estimate average thickness of the largest under-ice meltwater area as 52 cm, close to the estimates from FYI SIMBA and coring sites.

For SYI, the situation was different: a layer of under-ice meltwater (19–27 cm from mid-June until mid-July, 42–46 cm in late July, with average thickness of 26 ± 9 cm, n = 115) was only observed at the SIMBA location (**Figure 5b**), where SYI thickness was lower (1.17–1.78 m). At the SYI coring site with thicker ice (2.02–2.33 m)

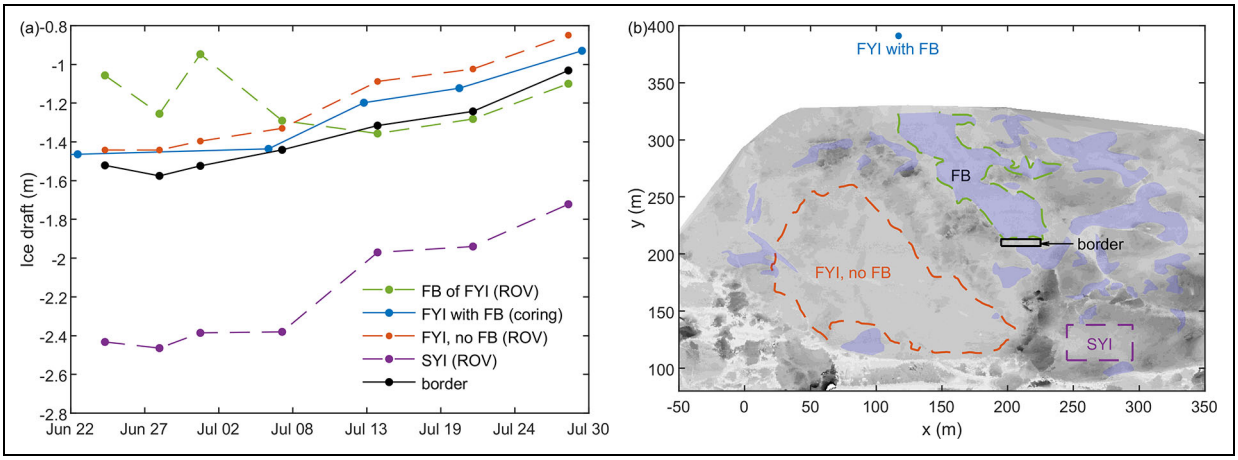

Figure 6. Ice draft evolution from remotely operated vehicle (ROV) multibeam sonar. (a) Draft evolution of false bottom (FB) below first-year ice (FYI), of FYI with and without false bottom, of second-year ice (SYI), and of the border between under-ice meltwater layers measured by ROV multibeam sonar, and (b) locations of corresponding ice types.

Table 1. Ice draft and ice draft change measured by coring and remotely operated vehicle (ROV) sonar, comparing first-year ice (FYI) with and without a false bottom (FB) and draft of the false bottom itself

	Draft (m)						Draft Change (m)			
	FYI				SYI		FYI		SYI	
	Coring	ROV	Coring	ROV	Coring	ROV	Coring	ROV	Coring	ROV
Date (2020)	With FB	No FB	FB	FB	No FB	No FB	With FB	No FB	No FB	No FB
May 04	1.61	—[a]	—	—	2.10	—	0.14	—	0.00	—
Jun 22–24	1.46	1.54	—	1.06	—	2.43	0.00	0.00	—	0.00
Jun 28	—	1.44	—	1.26	—	2.46	—	0.00	—	0.03
Jun 30–Jul 01	—	1.40	—	0.95	1.82	2.39	—	–0.05	–0.27	–0.05
Jul 06–07	1.44	1.33	1.78	1.29	2.01	2.38	–0.02	–0.11	–0.09	–0.05
Jul 13–14	1.20	1.09	1.72	1.36	2.45	1.97	–0.27	–0.35	–0.35	–0.46
Jul 20–21	1.12	1.02	1.75	1.28	1.81	1.94	–0.34	–0.42	–0.28	–0.49
Jul 28–29	0.93	0.85	1.24	1.10	—	1.72	–0.53	–0.59	—	–0.71

[a]Not available.

the meltwater only slightly affected the ice bottom temperature, warming it up to values from −1.4 to −1.7°C. No false bottoms were observed at the SYI coring site.

Mass balance

Effect of under-ice meltwater layers

In previous sections we defined the areal fraction and thickness temporal evolution of under-ice meltwater layers. To compare ice bottom melt for areas with and without under-ice meltwater layers, we combined observations from ROV sonar and from ice coring. FYI SIMBA and coring sites represent ice with under-ice meltwater layers. At the coring site from May 4 until July 29, FYI thickness decreased from its maximum value of 1.62 m to 1.07 m. During the melt season, the FYI SIMBA site became ponded, and thickness of ponded FYI decreased from 1.53 m to 0.71 m.

False bottoms were first observed at the FYI coring site on July 6, and their presence reduced FYI melt. The difference in accumulated ice melt between FYI with and without false bottom was 8–9 cm during July 6–21 and decreased to 6 cm by July 29. Based on combined ROV and coring measurements of FYI draft, FYI with the presence of false bottoms was 7–8% thicker (calculated as the difference in accumulated ice melt divided by the ice thickness). SYI was melting 16–27% faster than FYI without false bottoms and 29–52% faster than FYI with false bottoms, in the period of July 13–28 (**Figure 6a**). On average during three weeks of sonar observations, the difference in ice draft change relatively to SYI was 20 ± 4% smaller for FYI without false bottoms and 39 ± 10% smaller for FYI with false bottoms. A summary of ice draft changes measured by ice coring and by ROV multibeam sonar is presented in **Table 1**.

Table 2. Summer melt evolution for first-year ice (FYI) and second-year ice (SYI) coring and sea ice mass balance array (SIMBA) sites expressed in water equivalent, assuming snow density of 330 kg m^{-3} and ice density of 900 kg m^{-3}, and estimated under-ice meltwater layer thickness

	Water Equivalent (cm)										
	Unponded (Coring)					Ponded (SIMBAs)					
	Snow Melt		Total Melt		Meltwater Layer	Surface Melt		Bottom Melt		Meltwater Layer	
Date (2020)	FYI	SYI	FYI	SYI	FYI	FYI	SYI	FYI	SYI	FYI	SYI
May 04	– [a]	–	0	0	0	0	0	0	0	0	0
Jun 22	4	–	7	–	0	1	1	5	5	0	19
Jun 30	–	4	–	–	–	8	17	7	6	0	21
Jul 06	5	5	9	18	35	17	29	10	7	0	21
Jul 13	5	5	24	–	52	29	37	13	7	52	26
Jul 20	7	5	39	33	63	37	43	18	7	52	43
Jul 29	7	–	56	–	31	47	48	28	7	39	0

[a]Not available.

ROV sonar scans showed that the largest area with false bottoms was surrounded by thicker ice. We used this area, located at the border to another under-ice meltwater area (as shown in **Figure 6b**), to study ice draft of that thicker ice, surrounding the under-ice meltwater layer. The draft of this border was 1.6 m on June 28 and subsequently decreased until 1.0 m on July 28. When the average draft of the largest false bottom area reached its maximum value on July 14, its value became close to the draft of that border (**Figure 6a**), with a difference of 4 cm. During July 20–28, the difference between draft values of the largest false bottom area and that border was within 4–7 cm.

Meltwater balance and its horizontal transfer

In this section we compare observations of the under-ice meltwater layer with potential sources of meltwater including snowmelt, ice surface and bottom melt. All values are presented as water equivalents of meltwater thickness without considering the areal coverage of meltwater accumulations. The summary of ice mass balance for each of the weeks with coring events is presented in **Table 2** for May–July 2020. The values for unponded ice are from ice coring, while values for ponded ice are from SIMBAs. Total melt expressed as water equivalent includes one-dimensional ice top and bottom melt, as well as snow melt. Images of ice conditions at coring and SIMBA sites during the melt season are shown in the supplemental material (Figure S1).

Ponded areas produce more meltwater than unponded, but most of this additional meltwater is discharged into the mixed layer or stored in melt ponds (Eicken et al., 2002). We estimated surface melt pond coverage for the ROV area as 18% for July 1 (prior to false bottom appearance) using satellite imagery. Webster et al. (2022) showed that areal melt pond fraction was similar for FYI and SYI, while melt ponds formed on SYI were deeper. For the FYI area without false bottoms investigated in this study (**Figure 6b**), the melt pond fraction was 23%.

Maximum snow thickness at the FYI coring site was 21 cm in early May, after which it started to melt, and had completely disappeared by late July. In the areas where melt pond formation was registered by SIMBA temperature measurements later in the season, thinning of the snowpack started 1.5 months earlier, in early May, and proceeded until early June. Snow thickness before the melt season was around 18 cm for both FYI and SYI SIMBAs. The average snow thickness for the Central Observatory was measured in April as 14 cm at smooth level ice (Itkin et al., 2023).

The start of FYI bottom melt was observed on May 27, coinciding with FYI surface melt pond onset. Later these melt ponds were partially refrozen, and the total ice thickness loss was almost negligible. FYI melt ponds at the SIMBA site formed again one month later, on June 27. According to satellite imagery of the Central Observatory, subnivean melt ponds were present on June 17 and open melt ponds were present on June 21 (Webster et al., 2022). Rapid surface melt was initiated later, on July 6, together with under-ice meltwater layer formation on July 9. The meltwater at the SYI SIMBA site occurred on June 16, when the bottom melt of SYI was only 4 cm after approximately 1 month of slow melt.

On July 6, the total water equivalent of melted snow and ice at the FYI coring site was 4 times smaller than the under-ice meltwater layer thickness. This difference indicates that the under-ice meltwater was collected from a substantially larger area of melting ice. During July 13–29, the water equivalent of accumulated ice melt increased linearly from 24 cm to 45 cm, while the thickness of under-ice meltwater layer became relatively stable after July 13 for both FYI coring and SIMBA sites (**Figure 7a**). These results agree with ice draft measurements of thicker ice, surrounding under-ice meltwater

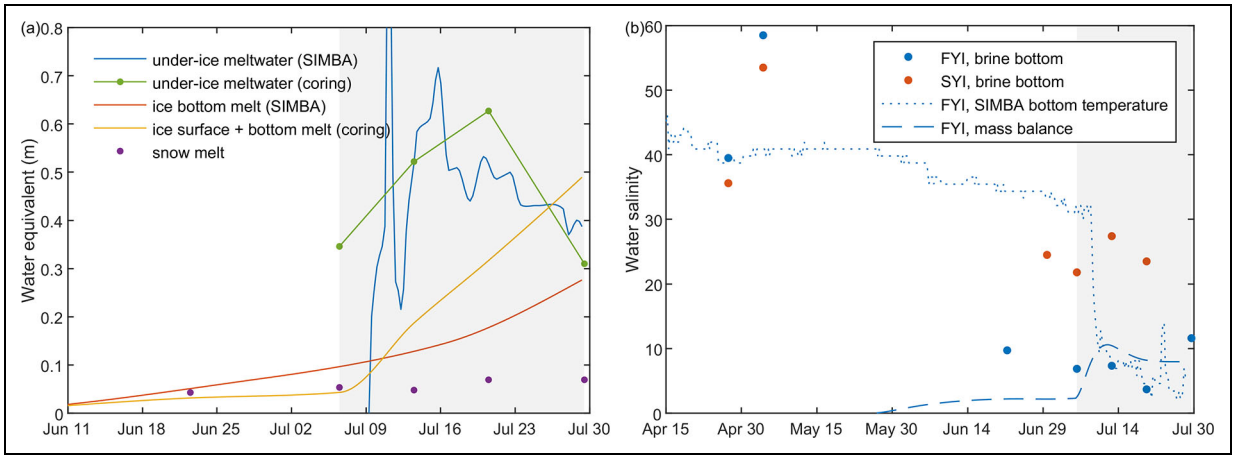

Figure 7. Water equivalents of melt sources and meltwater layers, and under-ice water salinity. (a) Thickness of under-ice meltwater layer (including false bottom), water equivalents of accumulated ice bottom and surface melt, and snow melt for first-year ice (FYI). (b) Brine salinity of ice bottom from FYI and second-year ice (SYI) coring, FYI under-ice meltwater salinity estimated from sea ice mass balance array (SIMBA) ice bottom temperature, and FYI under-ice meltwater salinity estimated from mass balance using Equation 1. The grey-shaded areas indicate the period with false bottoms at the FYI coring site.

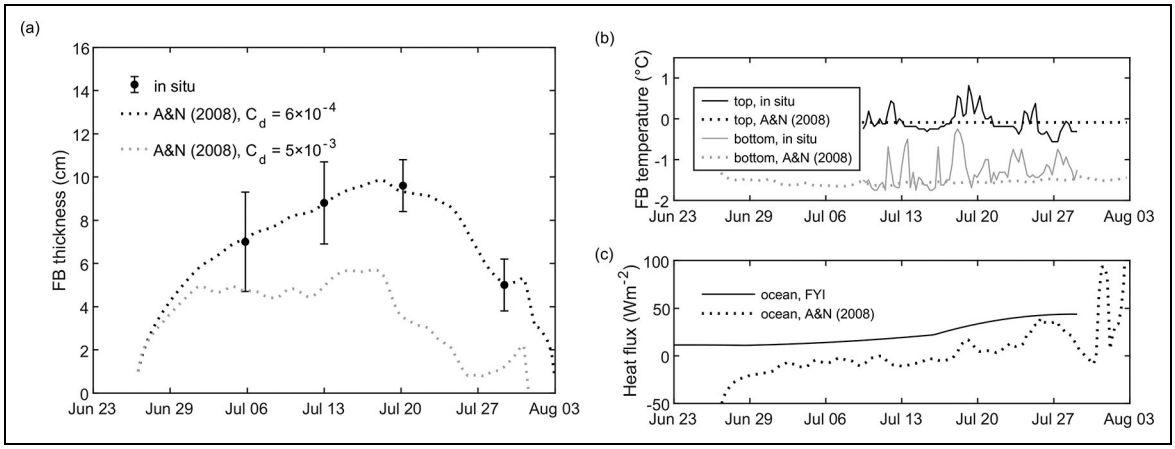

Figure 8. False bottom temperature, thickness, and ocean heat flux. We used the false bottom thermodynamic model from Alexandrov and Nizovtseva (A&N) (2008) with forcing from in situ measurements of drift speed, seawater temperature and salinity from *Polarstern*. (a) False bottom (FB) thickness, measured in situ at the first-year ice (FYI) coring site and estimated using the model, (b) top and bottom temperature of false bottom measured by FYI SIMBA and estimated using the model, and (c) ocean heat flux, estimated from FYI SIMBA measurements and from the model.

layers and limiting its depth after July 13 (**Figure 6a**). For SYI SIMBA site, the under-ice meltwater layer thickness was 4–6 times larger than the water equivalent of ice bottom melt.

False bottoms: Observations and modelling

The false bottoms at the FYI coring site were first observed on July 6 with an average thickness of 7 cm. Their thickness increased up to 10 cm after 1–2 weeks from when they were first observed, and then melted to 5 cm thickness after 3 weeks. The false bottoms at the FYI coring site slowly migrated upwards (0.5 cm day^{-1}) during the first 2 weeks of observation and started to migrate faster (4.7 cm day^{-1}) after July 19. The total lift of false bottoms of 54 cm was similar to the FYI draft decrease of 51 cm.

The thermodynamic model from Alexandrov and Nizovtseva (2008) was able to accurately describe false bottom thickness evolution (**Figure 8a**). Fer et al. (2022) reported an average value of friction velocity of 0.47 cm s^{-1} for MOSAiC observations and estimated an average value of ice-ocean drag coefficient C_d as 5×10^{-3}, which gives much higher average value of friction velocity of 1.65 cm s^{-1}, more than two times higher than measured by microstructure profiler in July. We found the best fit of in situ observations and model predictions of false bottom thickness for the average friction velocity of 0.57 cm s^{-1} and

Table 3. Ice and snow thickness, ice bulk salinity, temperature, and gas fraction for first-year ice (FYI) and second-year ice (SYI) coring (unponded) and sea ice mass balance array (SIMBA; ponded) sites

	Unponded (Coring)										Ponded (SIMBA)			
	Ice Thickness (m)		Salinity		Ice Temperature (°C)		Gas Fraction (‰)		Snow Thickness (m)		Ice Thickness (m)		Ice Temperature (°C)	
Date (2020)	FYI	SYI	FYI	SYI	FYI	SYI	FYI	SYI	FYI	SYI	FYI	SYI	FYI	SYI
May 04	1.62	2.33	5.2	2.4	−5.6	−5.7	11	11	0.21	0.12	1.53	1.78	−5.7	−5.5
Jun 22	1.59	—[a]	3.6	—	−1.2	—	17	—	0.08	—	1.47	1.72	−1.3	−1.0
Jun 30	—	2.04	—	1.0	—	−0.4	—	23	—	0.08	1.35	1.53	−1.1	−0.5
Jul 06	1.57	2.19	3.1	0.9	−0.7	−0.3	44	20	0.05	0.05	1.25	1.39	−1.0	−0.5
Jul 13	1.41	2.70	2.0	1.1	−0.5	−1.0	34	18	0.07	0.04	1.07	1.29	−0.7	−0.1
Jul 20	1.27	2.02	1.8	1.0	−0.4	−0.8	57	19	0	0.04	0.93	1.22	−0.5	−0.1
Jul 29	1.07	—	1.1	—	−0.4	—	63	—	0	—	0.71	1.17	−0.3	−1.4

[a]Not available.

corresponding ice-ocean drag coefficient of 6×10^{-4}. The results confirm our estimates of false bottom interface temperatures from SIMBA measurements (**Figure 8b**). Thermodynamic modelling demonstrated the key role of ocean heat flux in controlling the formation and thickness of false bottoms. We also found a substantial difference between the ocean heat flux below FYI and below false bottoms (**Figure 8c**); the increase of ocean heat flux below FYI is decreasing false bottom thickness, which is in agreement with the coupled simulations by Smith (2018). Meanwhile, the model from Alexandrov and Nizovtseva (2008) cannot accurately describe the evolution of false bottom draft, predicting its nearly constant upward migration, as the model does not consider limitations for the under-ice meltwater layer depth. The model from Alexandrov and Nizovtseva (2008) assumes zero ocean heat flux above the false bottom, which does not agree with our estimates of the ocean heat flux from the FYI SIMBA measurements and corresponding FYI bottom melt rates. Meanwhile, the negative values of the ocean heat flux from the model occurs at the same time (beginning of July) as the melt rate difference between FYI with and without false bottoms (**Figure 6a**).

Meltwater salt balance and sea ice physical properties

In this section we present the temporal evolution of FYI and SYI salinity, temperature, and density (**Table 3**). These parameters for unponded FYI and SYI were measured directly using ice coring (Tables S1 and S2), while temperatures of ponded FYI and SYI were measured continuously by SIMBAs. We used these measurements to calculate the total meltwater and salt mass balance.

Salt balance

The presence of under-ice meltwater has several effects on the temporal evolution of sea ice physical properties. It protects the ice from ocean heat flux and changes the water temperature below sea ice (**Figure 3b**). The effects of under-ice meltwater depend strongly on its salinity, which was measured at the ice-water interface (8 ± 3, $n = 4$) and also estimated from the ice-water interface temperature from SIMBA (7 ± 3, $n = 76$). The FYI bottom brine salinity, assumed to be equal to the under-ice meltwater salinity at the ice-water interface, was 4–12 during July, while SYI bottom brine salinity (22–27) was closer to seawater conditions (**Figure 7b**).

The salinity of the upper part of the under-ice meltwater layer was similar at FYI coring and SIMBA sites. We used measurements of FYI thickness and salinity to estimate the bulk salinity of the under-ice meltwater based on the mass balance of meltwater and salt (Equation 1). This mass balance gives an under-ice meltwater salinity of 8–11, with a substantial contribution from flushing of meltwater, reducing FYI salinity (**Figure 7b**). Direct measurements of under-ice meltwater layer salinity were in the same range and with a similar decreasing trend, until the meltwater became mixed with seawater on July 29.

We showed that the salinity changes of FYI substantially affected the salinity of under-ice meltwater by increasing it above the bulk salinity of melted ice. During winter and spring, the FYI bulk salinity was in the range 4.4–5.3 (Table S3), defined largely by the spatial variability of salinity (Figure S2b). From late April, the salinity started to decrease, and by the end of July, the bulk salinity of both FYI and SYI reached the range of 1.0–1.1 (**Table 3**).

During the freezing period until early May, the temperature profiles of FYI and SYI were almost linear (increasing towards the ice bottom with temperatures of seawater). During the melt period, the heat balance was affected by both shortwave radiation at the top and a relatively warm meltwater layer below the ice. At the end of June, the bottom half of the FYI became isothermal, and the upper half was linearly approaching 0°C. From the beginning of July, the FYI bottom temperature started to warm through the influence of the under-ice meltwater with the temperature between −0.2°C and −0.5°C. By mid-July, desalination affected the bottom 40 cm of FYI, while the surface

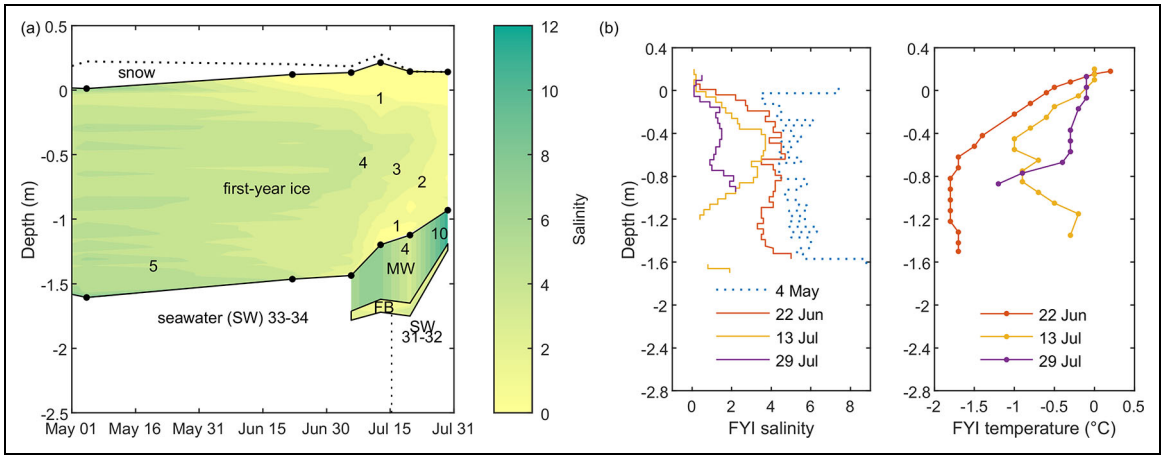

Figure 9. First-year ice (FYI) salinity evolution, and salinity and temperature profiles. (a) Salinity of FYI, under-ice meltwater layer (MW), and false bottom (FB) during melt season, and (b) temperature and salinity of FYI at the coring site during melt season, from ice coring.

55 cm started to lose salt due to flushing (**Figure 9b**). From mid-July, the middle part of the FYI slab also started losing salt. During the period July 13–20, there was still a cold middle section of about 50–60 cm with nearly constant temperatures and salinities. At the end of July, the FYI became almost isothermal in the range of 0 to −0.3°C except for the bottom 20 cm, affected by the colder meltwater at −1.2°C being more strongly mixed with seawater. This warming of the whole thickness of ice led to a substantial desalination of the middle-part to a salinity of 1.0–1.5. The bottom 20 cm experienced a linear increase in salinity from 1.0 to 2.2 due to the increased meltwater salinity.

Discussion

Under-ice meltwater layers: Spatial distribution and temporal evolution

The extent of under-ice meltwater layers was estimated as 20% from under-ice salinity profiles for five lines across the Central Observatory (Smith et al., 2022) and as 21% in this study. Despite good agreement in the average false bottom areal coverage, the study by Smith et al. (2022) showed a substantial variability of their presence, with almost no false bottoms in ridge areas and a substantial amount of false bottoms in areas with extensive surface melt ponds. This variability highlights the spatial heterogeneity in false bottom formation and its complex dependency on meltwater input and under-ice topography. It favors usage of three-dimensional mapping from ROV sonar for quantifying ice bottom topography over large areas of sea ice, as presented in our study. Additionally, Smith et al. (2022) reported an average thickness of under-ice meltwater layers of only 8 cm, while in our study those layers were on average 45–47 cm below FYI and 26 cm below SYI. This difference may be related to the choice of study area within the MOSAiC Central Observatory. For Smith et al. (2022), sampling transects were located close to the ice floe edges, which were located near lateral pond drainage channels (Webster et al., 2022). Additionally, the sampling areas with the presence of false bottoms were located under SYI in the Smith et al. (2022) study, where we observed thinner under-ice meltwater layers than below FYI.

We combined estimates of false bottom and surface melt pond locations to study their relationship. The areal extent of surface melt ponds for the area investigated in our study, was 18% on July 1, estimated from the satellite imagery (**Figure 10a**). Despite a good agreement in estimates of areal coverage of melt ponds above and under-ice meltwater layers below the ice, our data show that false bottoms occur only in areas of thin ice, encircled by thicker ice. We showed that such areas of level ice, surrounded by ridges, can be more than 50% covered by false bottoms, while level ice close to open water was found to have almost no false bottoms. For areas surrounded by ice ridges, there was good overlap between locations of false bottoms and surface melt ponds (**Figure 10a**). For the investigated area, surrounded by ice thicker than 1.7 m, the areal coverage of false bottoms was 63% and the areal coverage of surface melt ponds was 34%, of which 72% also had false bottoms (**Figure 10b**). Due to this additional condition for false bottom formation, the local areal coverage of false bottoms and surface melt ponds can differ despite the similar areal coverage for larger scales. Our observations indicate the importance of ridges for confining lateral meltwater movement under the ice, while surface melt ponds can also be formed in areas not encircled by thicker ice.

We can conclude that the emergence of false bottoms is linked to the bottom topography, with a higher likelihood for false bottoms to form under thinner ice surrounded by thicker ice areas. According to the satellite imagery, the FYI coring site and the largest under-ice meltwater area from ROV scans were surrounded by ridges and thicker ice. According to ROV sonar measurements, this thicker ice was limiting the depth of false bottoms and under-ice meltwater layers, which means that the rest of under-ice meltwater was transferred to the ocean mixed layer.

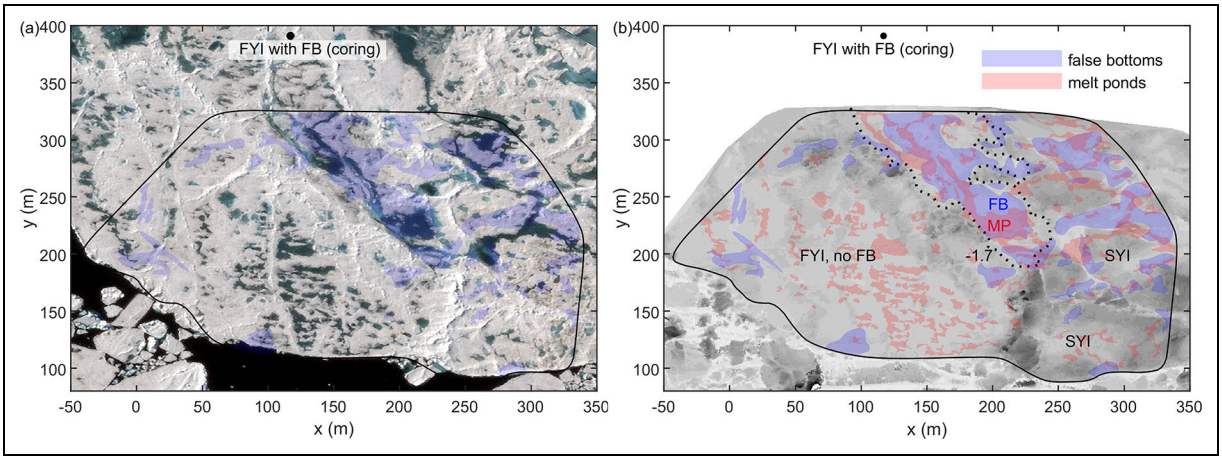

Figure 10. Locations of false bottoms and surface melt ponds. (a) Co-location of a satellite image of the ice floe from Planet Lab, Inc. (from Webster et al., 2022) and (b) ice draft from remotely operated vehicle (ROV) multibeam sonar, from July 1. Blue-shaded areas show estimate of false bottom (FB) coverage, and red-shaded areas show estimate of melt ponds (MP) within ROV scans. The ROV scan overlap area is encompassed by a solid black line.

Under-ice meltwater layers were stable during melt season for the MOSAiC expedition until the ice floe reached the ice edge on July 31. This study shows a substantial difference in timing of the main physical processes associated with melt for FYI and SYI. Surface melt ponds first formed on both FYI and SYI in late May (visible on May 28 in satellite imagery), formed ice lids and became snow covered at the beginning of June (no longer visible on June 3), and then underwent continual formation and evolution from mid-June (Webster et al., 2022). Based on the SIMBA data, other melt events occurred significantly earlier at the SYI site, compared to FYI. These events include bottom melt, which started at the SYI SIMBA site one month earlier in early June than the FYI SIMBA site. They also include surface melt ponds which formed on SYI one week earlier than on FYI, and did not refreeze. The formation of under-ice meltwater layers was also observed at SYI three weeks earlier than for FYI (June 16 and July 9, respectively). Ice type is thus shown to be one of the key factors defining the temporal evolution of under-ice meltwater layers.

Of interest is to compare these layers for MOSAiC and SHEBA. Our estimated areal fraction of under-ice meltwater layers (21%) is larger than the estimate of 15% for SHEBA (Perovich et al., 2003), while the thickness of surface melt ponds and under-ice meltwater layers was similar for MOSAiC and SHEBA. During the SHEBA expedition (Eicken et al., 2002), the under-ice meltwater layer thickness was increasing from 35 cm (June 1 to July 15) to 47 cm (July 16 to August 7). We estimated a thickness of under-ice meltwater layer for MOSAiC as 47 $\pm$ 14 cm (n = 81) below ponded FYI, 45 $\pm$ 15 cm (n = 4) below unponded FYI, and 26 $\pm$ 9 cm (n = 115) below ponded SYI. For MOSAiC, under-ice meltwater layers were first observed under SYI in mid-June, and under FYI in early July, both later than for SHEBA, which was located at a more southerly latitude during its melt season.

False bottoms and ice mass balance

Except for similar under-ice meltwater layer thickness, other physical parameters of under-ice meltwater and false bottoms differed between MOSAiC and SHEBA. The average false bottom thickness of 15 $\pm$ 5 cm at SHEBA was twice as large as at MOSAiC, where false bottom thickness was 8 $\pm$ 3 cm (n = 43). False bottoms at MOSAiC also had substantially higher salinities of 2.3 $\pm$ 0.5 (n = 10, Figure S2a), compared to 0.4 $\pm$ 0.4 at SHEBA (n = 35, Eicken et al., 2002). This difference cannot be explained by the ice salinity prior to melt season, being higher for SHEBA (4.5) than for the MOSAiC Central Observatory (3.2). This salinity difference suggests that under-ice meltwater was also substantially more saline for MOSAiC than for SHEBA.

False bottom presence reduced FYI melt, with 7–8% thicker FYI during July 6–29 compared to FYI of the same initial thickness but no false bottom. Differences of 1–8% of the final ice thickness were obtained by Smith (2018) using analytical modelling and a chosen range of several key parameters (meltwater salinity and depth, parent ice thickness, and ocean heat flux). The time of the largest differences in ice melt rates coincided with the time of the false bottom growth accompanied by substantial ocean heat fluxes, oriented from false bottoms towards the ocean (**Figure 8c**). In simulations by Smith (2018) there was a larger effect on sea ice thickening for under-ice meltwater layers with larger thickness, initial salinity, and initial false bottom thickness. A combination of areal coverage of false bottoms and their effect on ice melt rates, presented in our study, may give an estimate of the total contribution of this phenomenon on Arctic ice mass balance.

Meltwater and salt mass balance

According to ROV sonar measurements, the FYI coring site was representative for the MOSAiC Central Observatory in terms of both ice draft and melt rates. Our observations

(**Figure 7a**) show that the under-ice meltwater formation cannot be explained solely by one-dimensional balance of local meltwater sources: snow, ice surface and bottom melt. A horizontal transfer of under-ice meltwater from areas with thicker ice towards thinner ice is thus indicated. Due to relatively high salinity, the source of the under-ice meltwater layer cannot be related only to snow and ice melt and likely includes brine flushing. High salinities of under-ice meltwater support the measurements of low permeability and brine volume of false bottoms by Eicken (1994), and indicate that false bottoms trap brine entering the under-ice meltwater layer by flushing from the ice above. The under-ice meltwater salinity was 4–12 during July for MOSAiC, substantially higher than 1.5 measured during the ARCTIC 91 expedition by Eicken (1994).

A combination of thickness and areal fraction of under-ice meltwater layers together with snow and ice melt rates provides a mass balance of meltwater. For the SHEBA expedition (Eicken et al., 2002), by August 7 only 13% of the total surface meltwater volume remained in under-ice melt water layers, 30% in pond ice, and 26% in surface melt ponds. From our combined observations of FYI total melt, FYI meltwater layer thickness, and false bottom areal fraction, we estimate that around 17% of meltwater stayed in the under-ice meltwater layer by July 29. This estimate of meltwater mass balance shows how surrounding thicker ice while limiting under-ice meltwater thickness also defines the corresponding delay of the meltwater transfer from sea ice into the ocean mixed layer. Due to the higher areal fraction of under-ice meltwater during MOSAiC than during SHEBA, a higher fraction of the produced meltwater was stored for MOSAiC.

Both ice melt and desalination are coupled with under-ice meltwater salinity, so that understanding if ice salinities were typical for the melt season is important. Wang et al. (2020) presented ice salinity profiles for the Pacific Sector of the Arctic Ocean during August for several years between 2008 and 2018 and found a strong positive correlation between ice thickness and bulk salinity during the melt season, not observed in previous studies by Overgaard et al. (1983) and Tucker et al. (1987). For similar FYI thickness close to 1.1 m, their corresponding salinity was 1.8, which is substantially higher than for our study (1.1) in late July. For multiyear ice, the expected salinity, according to Wang et al. (2020), was 1.7, also almost twice as high as in our study (1.0). Meanwhile, ice conditions from Wang et al. (2020) were characterized by higher ice concentration and a larger distance from the open water in comparison to MOSAiC. Strong ice desalination during MOSAiC contributed to the high values of under-ice meltwater salinity in comparison to ARCTIC 91 expedition. The strong desalination can be supported by observations of lower salinity of ice with under-ice meltwater layers by Eicken (1994).

In our study we showed that the formation of false bottoms is affected by the following factors: surface melt ponds, melt pond flushing, areas of thin ice to collect meltwater, areas of thicker ice to constrain meltwater transfer to the mixed layer, and ocean heat flux. Areas with false bottoms, investigated by ROV sonar, had good overlap with areas with surface melt ponds (**Figure 10b**). The timing of false bottom appearance coincided well with the drainage of surface melt ponds (**Figure 2a**), which is supported by melt pond observations by Webster et al. (2022). False bottoms were formed in the areas of thin ice, encircled by thicker ice and ice ridges (**Figure 6b**). High values of ocean heat flux led to the melt of false bottoms (**Figure 8b**) and weakening water stratification under sea ice.

Thinner Arctic ice may result in increased ice dynamics, thus a higher probability of ice deformations and ridging (Itkin et al., 2017), which can create favorable conditions of ridge concentration for under-ice meltwater layers and false bottoms. More frequent appearance of false bottoms may lead to reduced ice melt for thin ice surrounded by ridges and thicker ice. It can also lead to the delayed transfer of salt and meltwater from sea ice to the ocean mixed layer. Faster melt rates of thicker ice and ridges, accompanied by delayed melt for thin ice with false bottoms, may reduce drag forces between sea ice and the ocean.

Summary and conclusions

This study presents an estimate of the areal coverage and temporal evolution of false bottoms and under-ice meltwater layers during the melt season from mid-June until late July 2020 during the MOSAiC expedition in the central Arctic. A combination of spatial coverage and temporal evolution of ice melt enabled us to calculate a total meltwater and salt mass balance for under-ice meltwater layers. We provided, for the first time using ROV multibeam sonar mapping, an estimate of the areal coverage of false bottoms below the ice as 21%. ROV surveys (350 by 200 m^2) indicated that ridge keels confine meltwater below the thinner ice, restrict lateral spreading, and prevent mixing with underlaying seawater, which results in the formation of distinct meltwater layers and false bottoms in areas of lower draft, which in turn changes ice melt rates and influences salt exchange between ice and ocean.

The average thickness of the under-ice meltwater layer was 45–47 cm below first-year ice (FYI) and 26 cm below second-year ice (SYI). Meltwater layers emerged instantly, and the thickness of the layer was not in balance with local snow and ice melt rates, pointing towards lateral transport and accumulation of meltwaters from a larger area. We registered a meltwater layer three weeks earlier below thin SYI compared to FYI with similar maximum thickness. Meltwater layers developed below both ponded and unponded FYI and below ponded and thinner SYI, while a meltwater layer did not appear below thicker and unponded SYI. Relatively high meltwater layer salinity (4–12) below FYI can be explained by brine flushed from FYI that is trapped above the false bottom, which was supported salt and meltwater mass balance and corresponding decreasing FYI salinity measurements from the ice coring.

A meltwater layer below FYI was first observed on July 6 at the coring site, this allowed the formation of false bottoms, which reduced FYI melt. After false bottoms

appeared, FYI with false bottoms was 7–8% thicker than FYI without false bottoms with the same initial thickness. Ice draft evolution measured by ROV from June 22 to July 28 showed that SYI (without false bottoms) melted 39% and 20% faster than FYI with and without false bottoms, respectively.

The mean weekly false bottom thickness was 5–10 cm for FYI with an average bulk salinity of 2.3 ± 0.5 during four weeks in July. Ice coring and SIMBA provided sufficient data to model growth and melt rates of false bottoms, which was mainly controlled by the oceanic heat flux below false bottoms. Meanwhile, our observations showed that ocean heat fluxes above false bottoms were non-zero as it is often assumed in thermodynamic models of false bottoms.

This study showed the impact of under-ice meltwater layers on the physical evolution of Arctic summer sea ice and its mass balance, indicated the conditions which support formation of under-ice meltwater layers, and assessed their areal coverage. The results indicate the importance of ridges for meltwater accumulation, which may occur more frequently in a thinner and more deformed ice pack. The observed differences in ice melt rates may lead to less spatial variability of sea ice after the melt season. The presented decrease in brine salinity at the bottom of FYI (when meltwater layers are present) can further play an important role for algae and microorganisms living near or at the ice-water interface.

Data accessibility statement

SkySat Imagery is courtesy of Planet Labs, Inc.

ROV multibeam sonar data: Katlein, C, Anhaus, P, Arndt, S, Krampe, D, Lange, BA, Matero, I, Regnery J, Rohde, J, Schiller, M, Nicolaus, M. 2022. Sea-ice draft during the MOSAiC expedition 2019/20. PANGAEA. DOI: https://doi.pangaea.de/10.1594/PANGAEA.945846.

SYI SIMBA: Lei, R, Cheng, B, Hoppmann, M, Zuo, G. 2021. Snow depth and sea ice thickness derived from the measurements of SIMBA buoy 2019T62. PANGAEA. DOI: https://doi.pangaea.de/10.1594/PANGAEA.938228.

FYI SIMBA: Lei, R, Cheng, B, Hoppmann, M, Zuo, G. 2021. Snow depth and sea ice thickness derived from the measurements of SIMBA buoy 2019T66. PANGAEA. DOI: https://doi.pangaea.de/10.1594/PANGAEA.938134.

MOSAiC oceanographical data:

Rex, M, Hoppmann, M, Tippenhauer, S, Rohardt, G. 2021. Continuous thermosalinograph oceanography along RV *POLARSTERN* cruise track PS122/1. PANGAEA. DOI: https://doi.org/10.1594/PANGAEA.930023.

Haas, C, Hoppmann, M, Tippenhauer, S, Rohardt, G. 2021. Continuous thermosalinograph oceanography along RV *POLARSTERN* cruise track PS122/2. PANGAEA. DOI: https://doi.org/10.1594/PANGAEA.930024.

Kanzow, T, Hoppmann, M, Tippenhauer, S, Rohardt, G. 2021. Continuous thermosalinograph oceanography along RV *POLARSTERN* cruise track PS122/3. PANGAEA. DOI: https://doi.org/10.1594/PANGAEA.930026.

Rex, M, Hoppmann, M, Tippenhauer, S, Rohardt, G. 2021. Continuous thermosalinograph oceanography along RV *POLARSTERN* cruise track PS122/4. PANGAEA. DOI: https://doi.org/10.1594/PANGAEA.930027.

MOSAiC meteorological data:

Cox, C, Gallagher, M, Shupe, M, Persson, O, Solomon, A, Ayers, T, Costa, D, Hutchings, J, Leach, J, Morris, S, Osborn, J, Pezoa, S, Uttal, T. 2021. Atmospheric Surface Flux Station #30 measurements (Level 1 Raw), Multidisciplinary Drifting Observatory for the Study of Arctic Climate (MOSAiC), central Arctic, October 2019–September 2020. Arctic Data Center. DOI: http://dx.doi.org/10.18739/A20C4SM1J.

Schmithüsen, H. 2021. Continuous meteorological surface measurement during *POLARSTERN* cruise PS122/1. Alfred Wegener Institute, Helmholtz Centre for Polar and Marine Research, Bremerhaven. PANGAEA. DOI: https://doi.org/10.1594/PANGAEA.935221.

Schmithüsen, H. 2021. Continuous meteorological surface measurement during *POLARSTERN* cruise PS122/2. Alfred Wegener Institute, Helmholtz Centre for Polar and Marine Research, Bremerhaven. PANGAEA. DOI: https://doi.org/10.1594/PANGAEA.935222.

Schmithüsen, H. 2021. Continuous meteorological surface measurement during *POLARSTERN* cruise PS122/3. Alfred Wegener Institute, Helmholtz Centre for Polar and Marine Research, Bremerhaven. PANGAEA. DOI: https://doi.org/10.1594/PANGAEA.935223.

Schmithüsen, H. 2021. Continuous meteorological surface measurement during *POLARSTERN* cruise PS122/4. Alfred Wegener Institute, Helmholtz Centre for Polar and Marine Research, Bremerhaven. PANGAEA. DOI: https://doi.org/10.1594/PANGAEA.935224.

Supplemental files

The supplemental files for this article can be found as follows:

Figures S1–S2. Tables S1–S3. Docx

Acknowledgments

This work was carried out and data used in this manuscript were produced as part of the international Multidisciplinary drifting Observatory for the Study of the Arctic Climate (MOSAiC) with the tag MOSAiC20192020. We thank all persons involved in the expedition of the Research Vessel *Polarstern* (Alfred-Wegener-Institut Helmholtz-Zentrum für Polar- und Meeresforschung, 2017) during MOSAiC in 2019–2020 (Project_ID: AWI_PS122_00) as listed in Nixdorf et al. (2021). Special thanks to those who contributed to the planning and organizing of the ice coring program, including Robert Rember, Hajo Eicken and Rolf Gradinger. We would especially like to acknowledge Marcel Nicolaus and Donald Perovich for their effort to coordinate the sea ice physics work during MOSAiC. Special thanks go to the people in the field; leg 1: Robert Rember, Jari Haapala, Nikolai Kolabutin, Egor Shymanchuk, Jian Ren, Michael Angelopoulos, Antonia Immerz, Jessie Creamean, Maria Josefa Verdugo, Lei Wang, Marcel Nicolaus, Dorothea Bauch, Sinhué Torres-Valdés; leg 2: Egor Shymanchuk, Igor Sheikin, Lasse M. Olsen, Adela Dumitrascu, Polona Itkin, Arttu Jutila, Daniela Krampe, Julienne Stroeve; leg 3: Jacqueline Stefels, Susanne Spahic, Anders Torstensson, Jeff Bowman, Igor Sheikin, Alexey Nubom,

and Laura Wischnewski; and leg 4: Igor Sheikin, Julia Regnery and Lisa Grosfeld. We thank Mario Hoppmann for the deployment of SIMBA buoys 2019T66 and 2019T62 and Lianna Nixon, Madison Smith, and Morven Muilwijk for providing photos of coring and SIMBA sites. We are grateful for the assistance of Nicholas C. Wright in processing of Planet Labs, Inc. Imagery. We also thank three anonymous reviewers that helped to improve the manuscript.

Funding

BAL, DD, ES, KVH, and MAG were supported by the Research Council of Norway through project HAVOC (grant no 280292). BAL and MAG were also supported by Research Council of Norway project CAATEX (grant no 280531) and MAG, DD, and MO by the Norwegian Polar Institute. AAF was supported by the AWI MOSAiC Coordination Project. SWF was supported by the NASA Cryospheric Sciences ISFM. DD's participation was also supported by EU H2020 project ARICE through the DEARice project teams berth fees (EU grant agreement No. 730695). IM was jointly supported by UKRI Natural Environment Research Council (NERC) and the German Federal Ministry of Education and Research (BMBF) through the Diatom ARCTIC project (BMBF Grant 629 03F0810A). CK received funding through the IceScan project (03F0916A) funded by the German Federal Ministry of Education and Research (BMBF). ROV operations, IM and CK received funding through the DiatomArctic project (NE/R012849/1; 03F0810A), part of the Changing Arctic Ocean program, jointly funded by the UKRI Natural Environment Research Council (NERC) and the German Federal Ministry of Education and Research (BMBF). ROV operations were further supported by the Helmholtz Infrastructure Initiative Frontiers in Arctic marine Monitoring (FRAM). RL was supported by the National Natural Science Foundation of China (41976219). GC was funded by the project *EcoLight* (03V01465) as part of the joint NERC/BMBF program Changing Arctic Ocean. DB was supported by the Netherlands Polar Programme (NWO), Project no 866.18.002. AR was supported by the German Research Foundation (DFG) through the Transregional Collaborative Research Center AC3 (268020496 TRR 172). AU was supported by the Swedish Research Council Formas (2018-01398). MO was supported by NSF OPP 1735862. EJC was supported by NSF OP OPP 1821911. CM was supported by NSF OPP 1753418. MW was supported by National Aeronautics and Space Administration's New Investigator Program in Earth Science (80NSSC20K0658) and the National Science Foundation (Project 2138786).

Competing interests

The authors declare that they have no conflict of interest.

Author contributions

Designed the ice coring program and allocated resources for the coring work: MAG, KVH, SM, MO, AAF.

Contributed to the collection of ice core data in the field: ES, BAL, RL, AAF, SWF, DD, MO, GC, DB, EJC, CJMH, OM, JG, AR, PSP, AU, CM.

Provided the SIMBA buoys: RL.

Contributed to the collection and processing of ROV multibeam sonar data: CK, IM.

Drafted the first draft of the manuscript: ES, KVH, MAG.

Contributed to drafting and to writing of the final version of the manuscript and approved the submitted version: All authors.

References

Aagaard, K, **Carmack, EC**. 1989. The role of sea ice and other fresh water in the Arctic circulation. *Journal of Geophysical Research* **94**(C10): 14485. DOI: http://dx.doi.org/10.1029/jc094ic10p14485.

Alexandrov, DV, **Nizovtseva, IG.** 2008. To the theory of underwater ice evolution, or nonlinear dynamics of "false bottoms." *International Journal of Heat and Mass Transfer* **51**(21–22): 5204–5208. DOI: http://dx.doi.org/10.1016/j.ijheatmasstransfer.2007.11.061.

Angelopoulos, M, **Damm, E**, **Simões Pereira, P**, **Abrahamsson, K**, **Bauch, D**, **Bowman, J**, **Castellani, G**, **Creamean, J**, **Divine, DV**, **Dumitrascu, A**, **Fons, SW**, **Granskog, MA**, **Kolabutin, N**, **Krumpen, T**, **Marsay, C**, **Nicolaus, M**, **Oggier, M**, **Rinke, A**, **Sachs, T**, **Shimanchuk, E**, **Stefels, J**, **Stephens, M**, **Ulfsbo, A**, **Verdugo, J**, **Wang, L**, **Zhan, L**, **Haas, C**. 2022. Deciphering the properties of different arctic ice types during the growth phase of MOSAiC: Implications for future studies on gas pathways. *Frontiers in Earth Science* **10**. DOI: http://dx.doi.org/10.3389/feart.2022.864523.

Assur, A. 1960. Composition of Sea Ice and its Tensile Strength. *SIPRE Research Report* **44**: 54.

Cox, GFN, **Weeks, WF.** 1983. Equations for determining the gas and brine volumes in sea-ice samples. *Journal of Glaciology* **29**(102): 306–316. DOI: http://dx.doi.org/10.3189/S0022143000008364.

Eicken, H. 1994. Structure of under-ice melt ponds in the central Arctic and their effect on, the sea-ice cover. *Limnology and Oceanography* **39**(3): 682–693. DOI: http://dx.doi.org/10.4319/lo.1994.39.3.0682.

Eicken, H, **Krouse, HR**, **Kadko, D**, **Perovich, DK**. 2002. Tracer studies of pathways and rates of meltwater transport through Arctic summer sea ice. *Journal of Geophysical Research: Oceans* **107**(10): 1–20. DOI: http://dx.doi.org/10.1029/2000jc000583.

Fer, I, **Baumann, TM**, **Koenig, Z**, **Muilwijk, M**, **Tippenhauer, S.** 2022. Upper-ocean turbulence structure and ocean-ice drag coefficient estimates using an ascending microstructure profiler during the MOSAiC drift. *Journal of Geophysical Research: Oceans* **127**(9). DOI: http://dx.doi.org/10.1029/2022JC018751.

Golden, KM, **Ackley, SF**, **Lytle, VI.** 1998. The percolation phase transition in sea ice. *Science* **282**(5397): 2238–2241. DOI: http://dx.doi.org/10.1126/science.282.5397.2238.

Griewank, PJ, **Notz, D.** 2013. Insights into brine dynamics and sea ice desalination from a 1-D model study of gravity drainage. *Journal of Geophysical Research:*

Oceans **118**(7): 3370–3386. DOI: http://dx.doi.org/10.1002/jgrc.20247.

Hanson, AM. 1965. Studies of the mass budget of arctic pack-ice floes. *Journal of Glaciology* **5**(41): 701–709. DOI: http://dx.doi.org/10.3189/s0022143000018694.

Itkin, P, **Hendricks, S**, **Webster, M**, **von Albedyll, L**, **Arndt, S**, **Clemens-Sewall, D**, **Jaggi, M**, **Oggier, M**, **Ricker, R**, **Rohde, J**, **Schneebeli, M**, **Liston, G**. 2023. Sea ice and snow mass balance from transects in the MOSAiC Central Observatory. *Elementa: Science of the Anthropocene*, **11**(1). DOI: https://doi.org/10.1525/elementa.2022.00048.

Itkin, P, **Spreen, G**, **Cheng, B**, **Doble, M**, **Girard-Ardhuin, F**, **Haapala, J**, **Hughes, N**, **Kaleschke, L**, **Nicolaus, M**, **Wilkinson, J.** 2017. Thin ice and storms: Sea ice deformation from buoy arrays deployed during N-ICE2015. *Journal of Geophysical Research: Oceans* **122**(6): 4661–4674. DOI: http://dx.doi.org/10.1002/2016JC012403.

Jackson, K, **Wilkinson, J**, **Maksym, T**, **Meldrum, D**, **Beckers, J**, **Haas, C**, **Mackenzie, D.** 2013. A novel and low-cost sea ice mass balance buoy. *Journal of Atmospheric and Oceanic Technology* **30**(11): 2676–2688. DOI: http://dx.doi.org/10.1175/JTECH-D-13-00058.1.

Jeffries, MO, **Schwartz, K**, **Morris, K**, **Veazey, AD**, **Krouse, HR**, **Gushing, S.** 1995. Evidence for platelet ice accretion in Arctic sea ice development. *Journal of Geophysical Research* **100**(C6): 10905. DOI: http://dx.doi.org/10.1029/95JC00804.

Katlein, C, **Schiller, M**, **Belter, HJ**, **Coppolaro, V**, **Wenslandt, D**, **Nicolaus, M**. 2017. A new remotely operated sensor platform for interdisciplinary observations under sea ice. *Frontiers in Marine Science* **4**(SEP): 1–12. DOI: http://dx.doi.org/10.3389/fmars.2017.00281.

Knust, R. 2017. Polar Research and Supply Vessel POLARSTERN operated by the Alfred-Wegener-Institute. *Journal of large-scale research facilities JLSRF* **3**: A119. DOI: http://dx.doi.org/10.17815/jlsrf-3-163.

Krumpen, T, **Birrien, F**, **Kauker, F**, **Rackow, T**, **Von Albedyll, L**, **Angelopoulos, M**, **Jakob Belter, H**, **Bessonov, V**, **Damm, E**, **Dethloff, K**, **Haapala, J**, **Haas, C**, **Harris, C**, **Hendricks, S**, **Hoelemann, J**, **Hoppmann, M**, **Kaleschke, L**, **Karcher, M**, **Kolabutin, N**, **Lei, R**, **Lenz, J**, **Morgenstern, A**, **Nicolaus, M**, **Nixdorf, U**, **Petrovsky, T**, **Rabe, B**, **Rabenstein, L**, **Rex, M**, **Ricker, R**, **Rohde, J**, **Shimanchuk, E**, **Singha, S**, **Smolyanitsky, V**, **Sokolov, V**, **Stanton, T**, **Timofeeva, A**, **Tsamados, M**, **Watkins, D.** 2020. The MOSAiC ice floe: Sediment-laden survivor from the Siberian Shelf. *Cryosphere* **14**(7): 2173–2187. DOI: http://dx.doi.org/10.5194/tc-14-2173-2020.

Lei, R, **Cheng, B**, **Hoppmann, M**, **Zhang, F**, **Zuo, G**, **Hutchings, JK**, **Lin, L**, **Lan, M**, **Wang, H**, **Regnery, J**, **Krumpen, T**, **Haapala, J**, **Rabe, B**, **Perovich, DK**, **Nicolaus, M.** 2022. Seasonality and timing of sea ice mass balance and heat fluxes in the Arctic transpolar drift during 2019–2020. *Elementa: Science of the Anthropocene* **10**(1). DOI: http://dx.doi.org/10.1525/elementa.2021.000089.

Leppäranta, M, **Manninen, T.** 1988. The brine and gas content of sea ice with attention to low salinities and high temperatures. Helsinki, Finland: Finnish Institute of Marine Research. Available at http://aquaticcommons.org/id/eprint/6760.

Malmgren, F. 1927. On the properties of sea ice, in *The Norwegian North Polar Expedition with the "Maud," 1918–1925*. Bergen, Norway: Scientific Results: 85.

Manes, SS, **Gradinger, R.** 2009. Small scale vertical gradients of Arctic ice algal photophysiological properties. *Photosynthesis Research* **102**(1): 53–66. DOI: http://dx.doi.org/10.1007/s11120-009-9489-0.

Maykut, GA. 1986. The surface heat and mass balance, in *The geophysics of sea ice*. Boston, MA: Springer: 395–463. DOI: http://dx.doi.org/10.1007/978-1-4899-5352-0_6.

Nansen, F. 1897. *Farthest North: Being the record of a voyage of exploration of the ship "Fram" 1893-96 and of a fifteen months' sleigh journey by Dr. Nansen and Lieut. Johansen* (vol. 2). New York, NY: Harper & Brothers. DOI: http://dx.doi.org/10.1037/12900-000.

Nicolaus, M, **Perovich, DK**, **Spreen, G**, **Granskog, MA**, **von Albedyll, L**, **Angelopoulos, M**, **Anhaus, P**, **Arndt, S**, **Belter, HJ**, **Bessonov, V**, **Birnbaum, G**, **Brauchle, J**, **Calmer, R**, **Cardellach, E**, **Cheng, B**, **Clemens-Sewall, D**, **Dadic, R**, **Damm, E**, **de Boer, G**, **Demir, O**, **Dethloff, K**, **Divine, DV**, **Fong, AA**, **Fons, S**, **Frey, MM**, **Fuchs, N**, **Gabarró, C**, **Gerland, S**, **Goessling, HF**, **Gradinger, R**, **Haapala, J**, **Haas, C**, **Hamilton, J**, **Hannula, H-R**, **Hendricks, S**, **Herber, A**, **Heuzé, C**, **Hoppmann, M**, **Høyland, KV**, **Huntemann, M**, **Hutchings, JK**, **Hwang, B**, **Itkin, P**, **Jacobi, H-W**, **Jaggi, M**, **Jutila, A**, **Kaleschke, L**, **Katlein, C**, **Kolabutin, N**, **Krampe, D**, **Kristensen, SS**, **Krumpen, T**, **Kurtz, N**, **Lampert, A**, **Lange, BA**, **Lei, R**, **Light, B**, **Linhardt, F**, **Liston, GE**, **Loose, B**, **Macfarlane, AR**, **Mahmud, M**, **Matero, IO**, **Maus, S**, **Morgenstern, A**, **Naderpour, R**, **Nandan, V**, **Niubom, A**, **Oggier, M**, **Oppelt, N**, **Pätzold, F**, **Perron, C**, **Petrovsky, T**, **Pirazzini, R**, **Polashenski, C**, **Rabe, B**, **Raphael, IA**, **Regnery, J**, **Rex, M**, **Ricker, R**, **Riemann-Campe, K**, **Rinke, A**, **Rohde, J**, **Salganik, E**, **Scharien, RK**, **Schiller, M**, **Schneebeli, M**, **Semmling, M**, **Shimanchuk, E**, **Shupe, MD**, **Smith, MM**, **Smolyanitsky, V**, **Sokolov, V**, **Stanton, T**, **Stroeve, J**, **Thielke, L**, **Timofeeva, A**, **Tonboe, RT**, **Tavri, A**, **Tsamados, M**, **Wagner, DN**, **Watkins, D**, **Webster, M**, **Wendisch, M**. 2022. Overview of the MOSAiC expedition. *Elementa: Science of the Anthropocene* **10**(1). DOI: http://dx.doi.org/10.1525/elementa.2021.000046.

Nixdorf, U, **Dethloff, K**, **Rex, M**, **Shupe, M**, **Sommerfeld, A**, **Perovich, D**, **Nicolaus, M**, **Heuzé, C**, **Rabe, B**, **Loose, B**, **Damm, E**, **Gradinger, R**, **Fong, A**, **Maslowski, W**, **Rinke, A**, **Kwok, R**, **Hirsekorn, M**, **Spreen, G**, **Mohaupt, V**, **Wendisch, M**, **Frickenhaus, S**, **Mengedoht, D**, **Herber, A**, **Immerz, A**, **Regnery, J**, **Weiss-tuider, K**, **Gerchow, P**, **Haas, C**, **König, B**, **Ransby, D**, **Kanzow, T**, **Krumpen, T**,

Rack, FR, **Morgenstern, A**, **Saitzev, V**, **Sokolov, V**, **Makarov, A**, **Schwarze, S**, **Wunderlich, T**. 2021. MOSAiC extended acknowledgement. *Zenodo*. DOI: http://dx.doi.org/10.5281/zenodo.5179739.

Notz, D, **McPhee, MG**, **Worster, MG**, **Maykut, GA**, **Schlünzen, KH**, **Eicken, H.** 2003. Impact of underwater-ice evolution on Arctic summer sea ice. *Journal of Geophysical Research: Oceans* **108**(7): 3223. DOI: http://dx.doi.org/10.1029/2001jc001173.

Notz, D, **Worster, MG**. 2008. In situ measurements of the evolution of young sea ice. *Journal of Geophysical Research* **113**(C3): C03001. DOI: http://dx.doi.org/10.1029/2007JC004333.

Overgaard, S, **Wadhams, P**, **Leppäranta, M**. 1983. Ice properties in the Greenland and Barents Seas during summer. *Journal of Glaciology* **29**(101): 142–164. DOI: http://dx.doi.org/10.1017/S0022143000005219.

Perovich, DK, **Grenfell, TC**. 1981. Laboratory studies of the optical properties of young sea ice. *Journal of Glaciology* **27**(96): 329–344. DOI: http://dx.doi.org/10.1017/s0022143000015410.

Perovich, DK, **Grenfell, TC**, **Richter-Menge, JA**, **Light, B**, **Tucker, WB**, **Eicken, H**. 2003. Thin and thinner: Sea ice mass balance measurements during SHEBA. *Journal of Geophysical Research: Oceans* **108**(3): 1–21. DOI: http://dx.doi.org/10.1029/2001jc001079.

Peterson, AK. 2018. Observations of brine plumes below melting Arctic sea ice. *Ocean Science* **14**(1): 127–138. DOI: http://dx.doi.org/10.5194/os-14-127-2018.

Pustogvar, A, **Kulyakhtin, A**. 2016. Sea ice density measurements. Methods and uncertainties. *Cold Regions Science and Technology* **131**: 46–52. DOI: http://dx.doi.org/10.1016/j.coldregions.2016.09.001.

Rinke, A, **Cassano, JJ**, **Cassano, EN**, **Jaiser, R**, **Handorf, D**. 2021. Meteorological conditions during the MOSAiC expedition: Normal or anomalous? *Elementa: Science of the Anthropocene* **9**(1): 1–17. DOI: http://dx.doi.org/10.1525/elementa.2021.00023.

Schmithüsen, H. 2021. Continuous meteorological surface measurement during POLARSTERN cruise PS122/4. *Alfred Wegener Institute, Helmholtz Centre for Polar and Marine Research, Bremerhaven*. PANGAEA. DOI: http://dx.doi.org/https://doi.org/10.1594/PANGAEA.935224.

Shupe, MD, **Rex, M**, **Blomquist, B**, **Persson, POG**, **Schmale, J**, **Uttal, T**, **Althausen, D**, **Angot, H**, **Archer, S**, **Bariteau, L**, **Beck, I**, **Bilberry, J**, **Bucci, S**, **Buck, C**, **Boyer, M**, **Brasseur, Z**, **Brooks, IM**, **Calmer, R**, **Cassano, J**, **Castro, V**, **Chu, D**, **Costa, D**, **Cox, CJ**, **Creamean, J**, **Crewell, S**, **Dahlke, S**, **Damm, E**, **de Boer, G**, **Deckelmann, H**, **Dethloff, K**, **Dütsch, M**, **Ebell, K**, **Ehrlich, A**, **Ellis, J**, **Engelmann, R**, **Fong, AA**, **Frey, MM**, **Gallagher, MR**, **Ganzeveld, L**, **Gradinger, R**, **Graeser, J**, **Greenamyer, V**, **Griesche, H**, **Griffiths, S**, **Hamilton, J**, **Heinemann, G**, **Helmig, D**, **Herber, A**, **Heuzé, C**, **Hofer, J**, **Houchens, T**, **Howard, D**, **Inoue, J**, **Jacobi, H-W**, **Jaiser, R**, **Jokinen, T**, **Jourdan, O**, **Jozef, G**, **King, W**, **Kirchgaessner, A**, **Klingebiel, M**, **Krassovski, M**, **Krumpen, T**, **Lampert, A**, **Landing, W**, **Laurila, T**, **Lawrence, D**, **Lonardi, M**, **Loose, B**, **Lüpkes, C**, **Maahn, M**, **Macke, A**, **Maslowski, W**, **Marsay, C**, **Maturilli, M**, **Mech, M**, **Morris, S**, **Moser, M**, **Nicolaus, M**, **Ortega, P**, **Osborn, J**, **Pätzold, F**, **Perovich, DK**, **Petäjä, T**, **Pilz, C**, **Pirazzini, R**, **Posman, K**, **Powers, H**, **Pratt, KA**, **Preußer, A**, **Quéléver, L**, **Radenz, M**, **Rabe, B**, **Rinke, A**, **Sachs, T**, **Schulz, A**, **Siebert, H**, **Silva, T**, **Solomon, A**, **Sommerfeld, A**, **Spreen, G**, **Stephens, M**, **Stohl, A**, **Svensson, G**, **Uin, J**, **Viegas, J**, **Voigt, C**, **von der Gathen, P**, **Wehner, B**, **Welker, JM**, **Wendisch, M**, **Werner, M**, **Xie, Z**, **Yue, F**. 2022. Overview of the MOSAiC expedition—Atmosphere. *Elementa: Science of the Anthropocene* **10**(1). DOI: http://dx.doi.org/10.1525/elementa.2021.00060.

Shupe, MD, **Rex, M**, **Dethloff, K**, **Damm, E**, **Fong, AA**, **Gradinger, R**, **Heuzé, C**, **Loose, B**, **Makarov, A**, **Maslowski, W**, **Nicolaus, M**, **Perovich, D**. 2020. The MOSAiC expedition: A year drifting with the Arctic. *NOAA Arctic Report Card*: 1–8. DOI: http://dx.doi.org/10.25923/9g3v-xh92.

Smith, MM, **von Albedyll, L**, **Raphael, IA**, **Lange, BA**, **Matero, I**, **Salganik, E**, **Webster, MA**, **Granskog, MA**, **Fong, A**, **Lei, R**, **Light, B**. 2022. Quantifying false bottoms and under-ice meltwater layers beneath Arctic summer sea ice with fine-scale observations. *Elementa: Science of the Anthropocene* **10**(1). DOI: http://dx.doi.org/10.1525/elementa.2021.000116.

Smith, N. 2018. Department of Meteorology Mathematical modelling of under-ice melt ponds and their impact on the thermohaline interaction between sea ice and the oceanic mixed layer. DOI: http://dx.doi.org/https://doi.org/10.48683/1926.00085363.

Timco, GW, **Weeks, WF**. 2010. A review of the engineering properties of sea ice. *Cold Regions Science and Technology* **60**(2): 107–129. DOI: http://dx.doi.org/10.1016/j.coldregions.2009.10.003.

Tsamados, M, **Feltham, D**, **Petty, A**, **Schroeder, D**, **Flocco, D**. 2015. Processes controlling surface, bottom and lateral melt of Arctic sea ice in a state of the art sea ice model. *Philosophical Transactions of the Royal Society A: Mathematical, Physical and Engineering Sciences* **373**(2052): 20140167. DOI: http://dx.doi.org/10.1098/rsta.2014.0167.

Tucker, WB, **Gow, AJ**, **Weeks, WF**. 1987. Physical properties of summer sea ice in the Fram Strait. *Journal of Geophysical Research* **92**(C7): 6787. DOI: http://dx.doi.org/10.1029/JC092iC07p06787.

Untersteiner, N. 1968. Natural desalination and equilibrium salinity profile of perennial sea ice. *Journal of Geophysical Research* **73**(4): 1251–1257. DOI: http://dx.doi.org/10.1029/JB073i004p01251.

Vancoppenolle, M, **Bitz, CM**, **Fichefet, T**. 2007. Summer landfast sea ice desalination at Point Barrow, Alaska: Modeling and observations. *Journal of Geophysical Research* **112**(C4): C04022. DOI: http://dx.doi.org/10.1029/2006JC003493.

Vancoppenolle, M, **Fichefet, T**, **Goosse, H**. 2009. Simulating the mass balance and salinity of Arctic and Antarctic sea ice. 2. Importance of sea ice salinity variations. *Ocean Modelling* **27**(1–2): 54–69. DOI: http://dx.doi.org/10.1016/j.ocemod.2008.11.003.

von Albedyll, L, **Haas, C**, **Dierking, W.** 2021. Linking sea ice deformation to ice thickness redistribution using high-resolution satellite and airborne observations. *The Cryosphere* **15**(5): 2167–2186. DOI: http://dx.doi.org/10.5194/tc-15-2167-2021.

Wang, Q, **Lu, P**, **Leppäranta, M**, **Cheng, B**, **Zhang, G**, **Li, Z**. 2020. Physical properties of summer sea ice in the Pacific sector of the Arctic during 2008–2018. *Journal of Geophysical Research: Oceans* **125**(9): 1–19. DOI: http://dx.doi.org/10.1029/2020JC016371.

Webster, MA, **Holland, M**, **Wright, NC**, **Hendricks, S**, **Hutter, N**, **Itkin, P**, **Light, B**, **Linhardt, F**, **Perovich, DK**, **Raphael, IA**, **Smith, MM**, **von Albedyll, L**, **Zhang, J**. 2022. Spatiotemporal evolution of melt ponds on Arctic sea ice. *Elementa: Science of the Anthropocene* **10**(1). DOI: http://dx.doi.org/10.1525/elementa.2021.000072.

Weeks, W. 2010. *On sea ice*. Fairbanks, AK: University of Alaska Press.

How to cite this article: Salganik, E, Katlein, C, Lange, BA, Matero, I, Lei, R, Fong, AA, Fons, SW, Divine, D, Oggier, M, Castellani, G, Bozzato, D, Chamberlain, EJ, Hoppe, CJM, Müller, O, Gardner, J, Rinke, A, Pereira, PS, Ulfsbo, A, Marsay, C, Webster, MA, Maus, S, Høyland, KV, Granskog, MA. 2023. Temporal evolution of under-ice meltwater layers and false bottoms and their impact on summer Arctic sea ice mass balance. *Elementa: Science of the Anthropocene* 11(1). DOI: https://doi.org/10.1525/elementa.2022.00035

Domain Editor-in-Chief: Jody W. Deming, University of Washington, Seattle, WA, USA

Guest Editor: Gunnar Spreen, Institute of Environmental Physics, University of Bremen, Bremen, Germany

Knowledge Domain: Ocean Science

Part of an Elementa Special Feature: The Multidisciplinary Drifting Observatory for the Study of Arctic Climate (MOSAiC)

Published: March 31, 2023 **Accepted:** February 13, 2023 **Submitted:** February 25, 2022

ELEMENTA Science of the Anthropocene

Elem Sci Anth is a peer-reviewed open access journal published by University of California Press.

OPEN ACCESS